ON THE SUB-SEASONAL PROCESSES CONTROLLING THE NATURAL PHYTOPLANKTON ABUNDANCE AND BIOLOGICAL PUMP IN THE DRAKE PASSAGE

by

Alexander Robert Davies

A thesis submitted to the Faculty of the University of Delaware in partial fulfillment of the requirements for the degree of Master of Science in Marine Studies

Summer 2015

ON THE SUB-SEASONAL PROCESSES CONTROLLING THE NATURAL PHYTOPLANKTON ABUNDANCE AND BIOLOGICAL PUMP IN THE DRAKE PASSAGE

by

Alexander Robert Davies

Approved: _____
Fabrice Veron, Ph.D.
Professor in charge of thesis on behalf of the Advisory Committee

Approved: _____
Matthew J. Oliver, Ph.D.
Professor in charge of thesis on behalf of the Advisory Committee

Approved: _____
Mark A. Moline, Ph.D.
Director of the School of Marine Science and Policy

Approved: _____
Nancy M. Targett, Ph.D.
Dean of the College of Earth, Ocean, and Environment

Approved: _____
James G. Richards, Ph.D.
Vice Provost for Graduate and Professional Education

ACKNOWLEDGMENTS

Foremost, I would like to express my sincere gratitude to my advisors Fabrice Veron and Matt Oliver. Fabrice thank you for your unwavering motivation, patience, and support in my academic, professional, and personal ventures. Your scientific knowledge in the area of air-sea interaction is unparalleled, and you undoubtedly shaped me into the scientist I am today. Matt thank you for broadening my academic horizons and pushing me to think critically as an interdisciplinary earth system scientist. I will carry the skills and knowledge I learned from you throughout the remainder of my career. Thank you both for your assistance in paper writing and with this thesis. While my original goal of earning a Ph.D. has not yet panned-out, I believe the ultimate end goal of an upper-level education is to develop the skills and knowledge needed to pursue a fun and fulfilling career. I can honestly say that I would not have developed those skills without mentoring from both you; for that, I am sincerely grateful and I could not have imagined a better set of academic advisors or professional mentors.

I would like to thank the Pablo Huq for serving on my M.S. Committee and for mentoring me academically and professionally throughout-out my tenure at Delaware, and now beyond. I'd also like to thank Denny Kirwan, Tobias Kukulka, Wade McGillis, and Bob Vaillancourt who all served on various versions of Ph.D. or M.S. Committee's throughout my academic program at the University of Delaware. Additional thanks to Ajoy Kumar and Richard Clark who advised and mentored me at Millersville University.

I would like to sincerely thank the POSE Fellowship program, the School of Marine Science and Policy, and the Robertson Donation/Graduate Fellowship fund for supporting my studies at the University of Delaware. I'd like to further thank the University of Delaware Office of Graduate and Professional Education, along with the

School of Marine Science and Policy and the Robertson Donation fund, for supporting my participation in 2013 SOLAS Summer School in Xiamen, China.

I'd like to thank all my class- and lab- mates in the Air-Sea Interaction Lab, the Ocean Exploration, Remote Sensing, and Biogeography Lab, and 210 Robinson Hall. I will always be grateful for the leadership and guidance offered by Joseph Senne and Phil Muscarella early in my academic program. Thank you to Pat Ryan, Joe Brodie, Justin Gilchirst, Tyler Rabe, Auvi Rahman, and all POSE students for not only enriching me academically, but also helping me keep my sanity during the tough and stressful patches. Thank you to Megan Cimino, Danielle Haulsee, and Matt Breece for welcoming me into your lab and unselfishly sharing your collective knowledge and experience with me.

Last but not least, I would like to thank my family. Thank you Chelsea for your unwavering love and support. You lifted my spirit on all of those earlier mornings following late nights in the office, and continuously motivating me to persevere through all the ups and downs. After the chapters in this thesis are finalized, I look forward to writing the next chapters of my life with you and our new family. Thank you to my parents for encouraging me to pursue my goals and dreams at every stage of my life. All of your hard work, love, and support has shaped me into the man I am today. Thank you for your support throughout my academic career, dating back to my first day at Millersville University. Thank you to Pat and Larry Keckler for encouraging me and supporting Chelsea through out this process. Finally, thank you to my brother, sisters, friends, and extending family for all of your love and support.

TABLE OF CONTENTS

LIST OF TABLES

LIST OF FIGURES

ABSTRACT

The biological pump is an important aspect of the global carbon cycle. Phytoplankton blooms in the surface ocean draw down atmospheric carbon dioxide and package it as organic particulates that sink into the deep ocean, where carbon can be sequestered on millennial timescales. Phytoplankton blooms are controlled by nutrient availability, changes in light exposure, respiration, and grazing. In the high nitrate, low chlorophyll surface waters of the open Southern Ocean (SO), blooms are further limited by insufficient iron concentrations. Hence, the SO draws considerable attention as a potential site for geoengineered atmospheric carbon concentrations via iron fertilization. However, there are no prolonged, in-situ observations of the mechanisms controlling the formation of naturally occurring phytoplankton blooms in the SO. To better understand the bloom formation mechanisms in the SO, an APEX biofloat was deployed in the energetic Drake Passage. The biofloat profiled the water column every two days and resolved the development of a natural phytoplankton bloom, along with a subsequent organic carbon export event. Satellite observations suggest that the phytoplankton abundance in the Drake Passage is low when the surface mesoscale kinetic energy (KE) is high. This observation is supported by biofloat observations that revealed, on average, high levels of KE deepen the mixed layer and may therefore control phytoplankton abundance through light limitation. Satellite observations further suggest that the relationship between high KE and phytoplankton abundance could be extended to the entire SO. Furthermore, our analysis indicates that when the high mesoscale kinetic energy control on phytoplankton abundance is alleviated, the mechanisms important for natural bloom formation include sub-mesoscale grazing relaxation and foreign iron deposition. Following the bloom, we infer that high levels of mesoscale kinetic energy contributed to organic carbon export.

Chapter 1

INTRODUCTION

1.1 Background

Covering roughly 70% of the Earth's surface, the play a major role in the global carbon cycle. On multi-decadal time scales, the deep ocean acts as a significant sink of natural and anthropogenic atmospheric carbon dioxide (Raven and Falkowski, 1999; Sabine et al., 2004; Gruber et al., 2009). Indeed, from the beginning of the 19th century through the 20th century, the oceans have sequestered 48% of anthropogenic atmospheric carbon dioxide (Sabine et al., 2004), making them an important carbon reservoir. The mechanisms driving the oceanic sequestration of atmospheric carbon are complex and require both physical and biochemical processes operating over a range of temporal and spatial scales.

Molecular diffusion is the dominant process controlling carbon dioxide (CO_2) flux across the coupled, atmosphere-ocean interface. The magnitude of the air-sea partial pressure of CO_2 (pCO_2) gradient is proportional to the exchange rate with gas flux possible in either direction (in or out of the surface ocean depending on the direction of the gradient). Unlike atmospheric pCO_2 values, surface ocean values of pCO_2 can vary on relatively short temporal and spatial scale between 150 and 550 μatm (Takahashi et al., 2002). Hence, the pCO_2 gradient (ΔpCO_2) is primarily set by the surface ocean with variations due to seasonal changes in temperature, biogeochemical processes, and the upwelling of deep ocean waters that contain a high concentration of CO_2 (Takahashi et al., 2002). As shown in Figure (1.1), the strongest positive ΔpCO_2 values (i.e. a source of CO_2 for the atmosphere) occur year-round along the Pacific equatorial region, and to a lesser extent, the Atlantic equatorial region. The

coherence in latitude of the positive ΔpCO_2 feature is likely due to the consistently warm low latitude temperatures, however the equatorial Pacific is also an upwelling zone for respired deep ocean CO_2. Meanwhile the South Atlantic and Southern Ocean regions, along with the North Atlantic are, on average, a sink for atmospheric CO_2 almost year-round.

In addition to molecular diffusion and the variability in ΔpCO_2 values, air-sea gas flux is also dependent on the wind stress (Ho et al., 2011). Wind generated turbulence on both sides of the interface can erode the height of the diffusive-molecular layer which enhances gas exchange because the "bulk" gas concentrations are effectively closer to the air-sea interface. Furthermore, the wind also increases gas exchange via wave breaking and bubble entrainment (Farmer et al., 1993).

However, the atmosphere and surface ocean exchange CO_2 on relatively short timescales; the turnover time for atmospheric CO_2 in the surface ocean is only on the order of one to ten years. Hence, variability in air-sea gas flux mechanisms, when taken in isolation, are largely inconsequential with regard to the long-term oceanic sequestration of atmospheric CO_2 on climatic time scales. In contrast, the deep ocean can sequester carbon on the order of 100–1,000 years (Ciais et al., 2013), making it an important long-term sink for atmospheric CO_2. Therefore, the oceanic sequestration of atmospheric CO_2 depends not only on the relatively quick exchange of CO_2 between the atmosphere and surface ocean, but also upon the the transport of carbon from the surface to deep ocean. The pycnocline (a region of rapidly changing density with depth) limits vertical exchanges between the surface and deep ocean, and subsequently acts to retard the deep ocean sequestration of atmospheric CO_2.

The biological pump is one mechanism by which atmospheric CO_2 is transported across the pycnocline and into the deep ocean. In well lit, nutrient rich regions of the surface ocean phytoplankton act to draw down atmospheric CO_2 by converting it into particulate organic carbon through oxygenic photosynthesis. Specifically, photosynthesis is an oxidation-reduction reaction that converts light energy into chemical bond

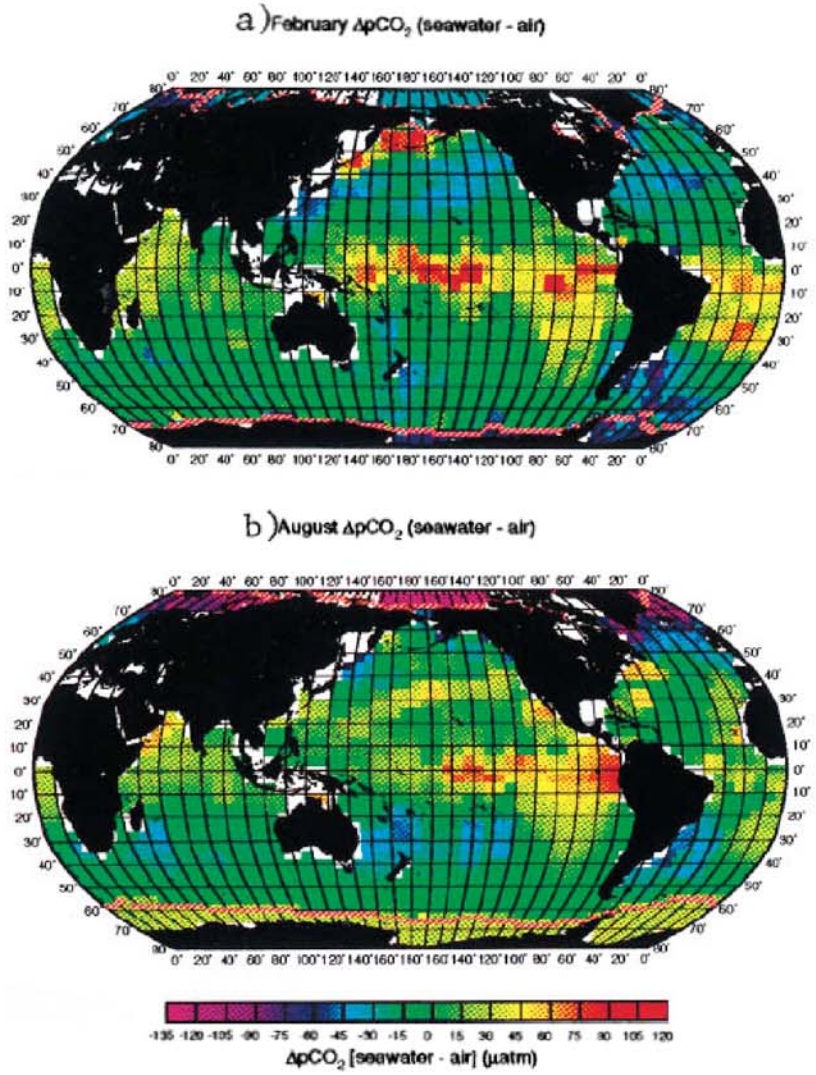

Figure 1.1: Mean monthly distribution of ΔpCO_2 (μatm) for *a)* February 1990 and *b)* August 1990 from Takahashi et al. (1997)

energy in the form of organic compounds (Falkowski and Raven, 2007). In Photosynthesis, the electron and proton recipient is CO_2 which is converted to organic carbon via carbon fixation. As presented in Falkowski and Raven (2007), photosynthesis is

$$CO_2 + 2H_2O + \text{Light} \xrightarrow{\text{chlorophyll-}a} CH_2O + H_2O + O_2, \tag{1.1}$$

where chlorophyll-a is a photosynthetic pigment found in most oxygenic photosynthetic organisms. Chlorophyll-a absorbs light energy and acts as an electron catalyst in the photosynthetic reduction reaction (Falkowski and Raven, 2007). If not respired by other trophic levels, phytoplankton blooms senesce, aggregate by cell-to-cell coalescence or in zooplankton fecal pellets, and sink into the deep ocean. In the deep ocean, phytoplankton aggregates are either converted back to dissolved inorganic CO_2 through microbial decomposition or are buried in the deep-ocean sediments on millennial timescales (Ciais et al., 2013).

1.2 Motivation

The relative importance of the Southern Ocean (SO) in the oceanic draw down of atmospheric carbon dioxide (CO_2) remains understudied and unresolved. Estimates suggest the Southern Ocean (SO) could account for anywhere between a tenth and a quarter of annual global ocean carbon uptake (Takahashi et al., 2002; Roy et al., 2003; McNeil et al., 2007). Despite the uncertainty, modeling experiments suggest the SO will continue to play a major role in oceanic carbon uptake over the coming century (Sarmiento et al., 1998; Orr et al., 2001). As the earth continues to warm over the next 100 years (IPCC, 2013), the SO is expected to become more stable and hence, the biological pump's role SO carbon sequestration is forecast to enhance relative to the solubility pump (Sarmiento et al., 1998).

The SO is a high latitude ecosystem and phytoplankton are seasonally light limited (El-Sayed, 1987). In austral summer, the surface waters of the open SO are generally macro-nutrient (e.g. nitrogen and phosphorous) rich, yet the standing stock

of phytoplankton is characterized by patchy, intense blooms within a generally unproductive environment (Moore and Abbott, 2000; Arrigo et al., 2008). Iron injection experiments (Boyd et al., 2000; Gervais et al., 2002; Coale et al., 2004; Hoffmann et al., 2006) suggest the patchy nature of the SO phytoplankton abundance is explained by low surface ocean dissolved iron concentrations. While iron is likely a major limiting factor for SO blooms, the mechanisms controlling phytoplankton abundance and the biological pump in the SO remain unresolved. This study, the MUltisensor STability And CHlorophyll Experiment (MUSTACHE), further investigates bloom formation mechanisms in the SO through the deployment of an Autonomous Profiling EXplorer (APEX biofloat) in the Drake Passage. Chapter two outlines the encompassing methodology used in this study; chapter-specific methodology is introduced by chapter. Chapter three investigates mesoscale kinetic energy as a potentially limiting factor on SO phytoplankton abundance. Chapter four discuses the sub-mesoscale mechanisms driving a naturally occurring phytoplankton bloom and organic carbon export event.

Chapter 2

METHODS

2.1 APEX Float

The MUSTACHE APEX float was deployed in the Drake Passage on December 18, 2012 at 64.813 ^{o}W and 59.870 ^{o}S. The float collected data from January 10 to June 4, 2013 (the observational period) as it profiled the water column from 2,000 dbar to the surface, every two days. Figure (2.1) shows the float trajectory and surface locations during the observational period.

APEX floats move vertically through the water column via small changes in their overall volume, and hence their buoyancy. The floats are equipped with an internal oil reservoir with 200 cubic centimeters (cc) of oil; the oil density is $0.8585\,\mathrm{g\,cc^{-1}}$. A hydraulic piston adds (or subtracts) oil into a partially evacuated pressure casing or bladder that results in a change in volume (but not mass). The mass of the instrument is around 26.5 kg when ready to deploy.

The ascent from the profiling depth to the surface is initiated when the hydrological piston is nudged by 22 counts. Each piston count pushes 1.2 grams of oil into the external bladder. After the initial nudge, additional buoyancy nudges are applied through the accent every time the accent rate drops below $0.08\,\mathrm{dbar\,s^{-1}}$. Buoyancy nudges are typically five counts and are applied as needed until the float surfaces. The reverse process (drawing oil out of the external bladder and back into the internal reservoir) occurs during decent.

Figure (2.2) shows the typical sampling cycle for an APEX float. In Figure (2.2), cycle beings with decent from the surface to the park depth, around 1,000 dbar. The decent marks the beginning of "down time" in the sampling cycle. The float remains at

the park depth for a programmable period of time, typically nine days for most APEX float deployments. For the fast profiling frequency in MUSTACHE, the float was at park depth for 22 to 26 hours. After the programmed period of time at the park depth has elapsed, the float descends to the "profiling depth," near 2,000 dbar. The float remains near 2,000 dbar until it is neutrally buoyant with respect to the environment (typically a couple hours). The "up time" period in the sampling cycle begins as the float ascends from the profiling depth to the surface. As the float ascends, the instrument payload samples the water column. When the float arrives at the surface it connects with an Iridium Satellite and relays the data (including the GPS position) in near real-time. After the data has been successfully transmitted, the sampling cycle repeats itself. The "down time" associated with a typical APEX float deployment is approximately 9.5 days with an "up time" of approximately half a day; the exact duration of down and up time can vary due to ascent/descent rates. In comparison, the "down time" associated with the MUSTACHE float is approximately 1.5 days with an "up time" of approximately half a day.

For this study, the MUSTACHE float made measurements at discrete sampling depths during ascent to the surface. Below 1000 dbar measurements were made approximately every 100 dbar, between 1000 and 500 dbar measurements were made approximately every 50 dbar, and above 500 dbar measurements were made approximately every 5 dbar for a high resolution sampling of the upper ocean. Table (2.1) lists the discrete sampling depths.

The MUSTACHE APEX float is deemed a "biofloat" because it measured vertical profiles of both physical and biochemical water column properties. The biofloat was equipped with a SeaBird model 41 CTD that measured the temperature (T °C), the salinity (S psu), and the pressure (P dbar). The temperature and salinity profiles are used to calculate profiles of $\sigma_t = \rho$ - 1,000, where ρ is the density calculated as a function of temperature and salinity only (Gill, 1982):

Spot Sampling Depths (dbar)							
2000	1900	1800	1700	1600	1500	1400	1300
1200	1100	1000	950	900	850	800	750
700	650	600	550	500	495	490	485
480	475	470	465	460	455	450	445
440	435	430	425	420	415	410	405
400	395	390	385	380	375	370	365
360	355	350	345	340	335	330	325
320	315	310	305	300	295	290	285
280	275	270	265	260	255	250	245
240	235	230	225	220	215	210	205
200	195	190	185	180	175	170	165
160	155	150	145	140	135	130	125
120	115	110	105	100	95	90	85
80	75	70	65	60	55	50	45
40	35	30	25	20	15	10	5

Table 2.1: APEX float discrete sampling depths (dbar). A single measurement is taken (roughly) at each pressure mark during the float ascent from the profiling depth to the surface. As a quick approximation, the pressure in dbar and the depth in meters are roughly equal.

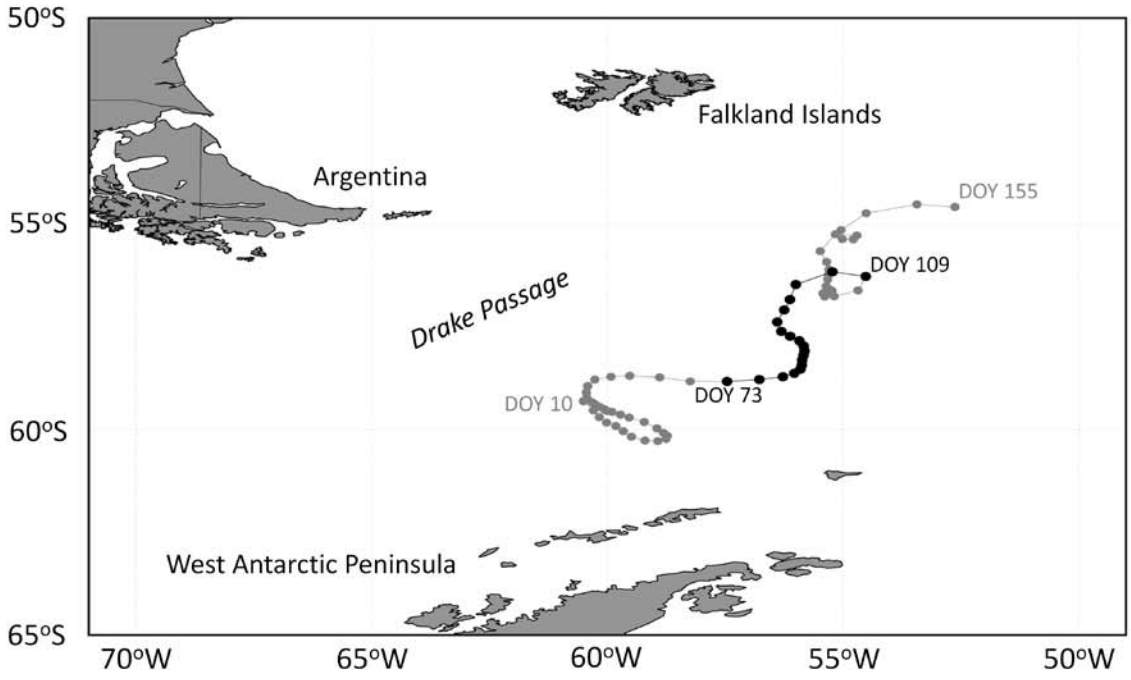

Figure 2.1: APEX float trajectory during the observational period (gray) and bloom-export period (black).

$$\begin{aligned}
\rho &= \rho_{fresh} + S\left(0.824493 - 4.0899T \times 10^{-3}\right) \\
&+ S\left(7.6438T^2 \times 10^{-5} - 8.2467T^3 \times 10^{-7} + 5.3875T^4 \times 10^{-9}\right) \\
&- S^{1.5}\left(5.72466 \times 10^{-3} + 1.0227T \times 10^{-4} - 1.6546T^2 \times 10^{-6}\right) \\
&+ S^2\left(4.8314 \times 10^{-4}\right) \qquad (2.1)
\end{aligned}$$

In Equation (2.1), ρ_{fresh} is the density of fresh water,

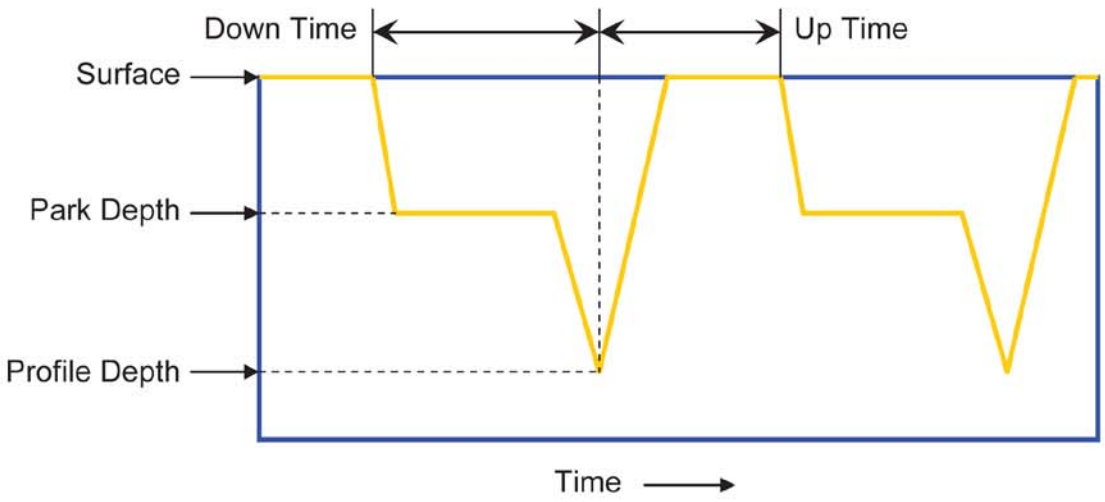

Figure 2.2: APEX float sampling cycle. This is the sampling cycle used by the MUSTACHE APEX float where the total time cycle time (down time and up time) is approximately two days. The park depth is 1,000 dbar and the profile depth is 2,000 dbar. This figure is courtesy Webb Research (2012)

$$\begin{aligned} \rho_{fresh} &= 999.842594 + 6.793952T \times 10^{-2} - 9.095290T^2 \times 10^{-3} \\ &+ 1.001685T^2 \times 10^{-4} - 1.120083T^4 \times 10^{-6} \\ &+ 6.536332T^5 \times 10^{-9}. \end{aligned} \tag{2.2}$$

By integrating the hydrostatic equation, the biofloat sampling pressures (Table 2.1) are converted to sampling depths, z (m). For this conversion, I assumed a standard atmosphere of pressure at the ocean surface as the upper boundary condition.

The salinity, temperature, and σ_t data profiles are linearly interpolated onto a fixed grid. The vertical extent of the grid is from 10 m to 1800 m depth with vertical spacing of 0.5 m. The gridded temperature, salinity, and σ_t contoured profiles plots between DOY 31 and 139 are shown in Figures (2.3), (2.4), and (2.5), respectively. For the analysis in Chapters (3) and (4), the profile DOY 71 was eliminated from

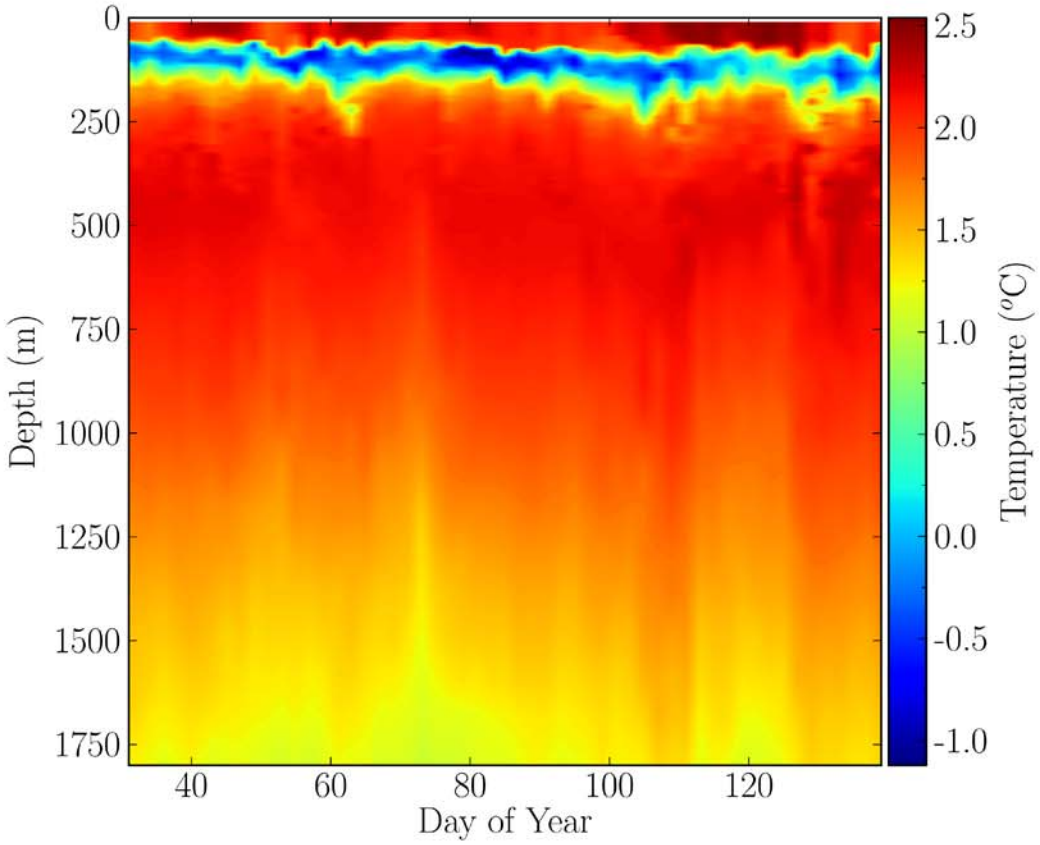

Figure 2.3: Gridded temperature signal in °C. The temperature is measured by the biofloat at sampling depths found in Table (2.1) and linearly interpolated to grid from 10 m to 1,800 m depth with a 0.5 m resolution.

consideration as it exhibited unrealistic and noisy salinity and σ_t inversions, clearly seen in the upper 500 m in Figures (2.4) and (2.5). This may have been due to a temporary blockage in the conductivity cell on that profile. The profile on DOY 71 is included in all plots in Chapter (2) to show this feature.

The biofloat was also equipped with a WET Labs Combination Fluorometer-Scattering-CDOM Sensor model ECO FLbbCD-AP2 that measured chlorophyll-a fluorescence (proxy for phytoplankton abundance), colored dissolved organic matter (CDOM) florescence, and volume backscattering (particle concentration). The signal output

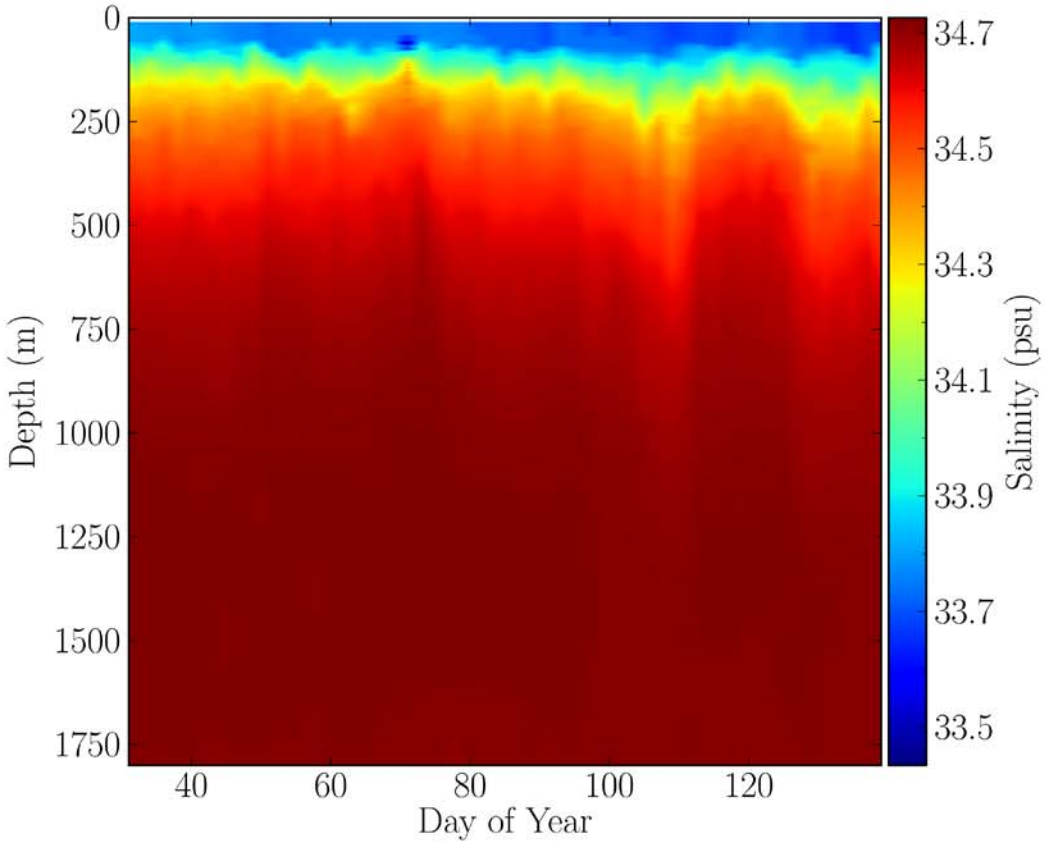

Figure 2.4: Gridded salinity signal in psu. The salinity is measured by the biofloat at sampling depths found in Table (2.1) and linearly interpolated to grid from 10m to 1,800m depth with a 0.5 m resolution.

from the chlorophyll-a flourometer and CDOM flourometer was in "counts." The WET-Lab calibration sheet provides the conversion from signal output to chlorophyll-a concentrations (μgl^{-1}) and CDOM concentration (ppb). The conversions are in Equations (2.3) and (2.4), respectively. The biofloat surfaced at night to reduce the effects of non-photochemical quenching on chlorophyll-a florescence measurements.

$$[\text{Chl}] = 0.0073(\text{Counts}_{output} - 50) \tag{2.3}$$

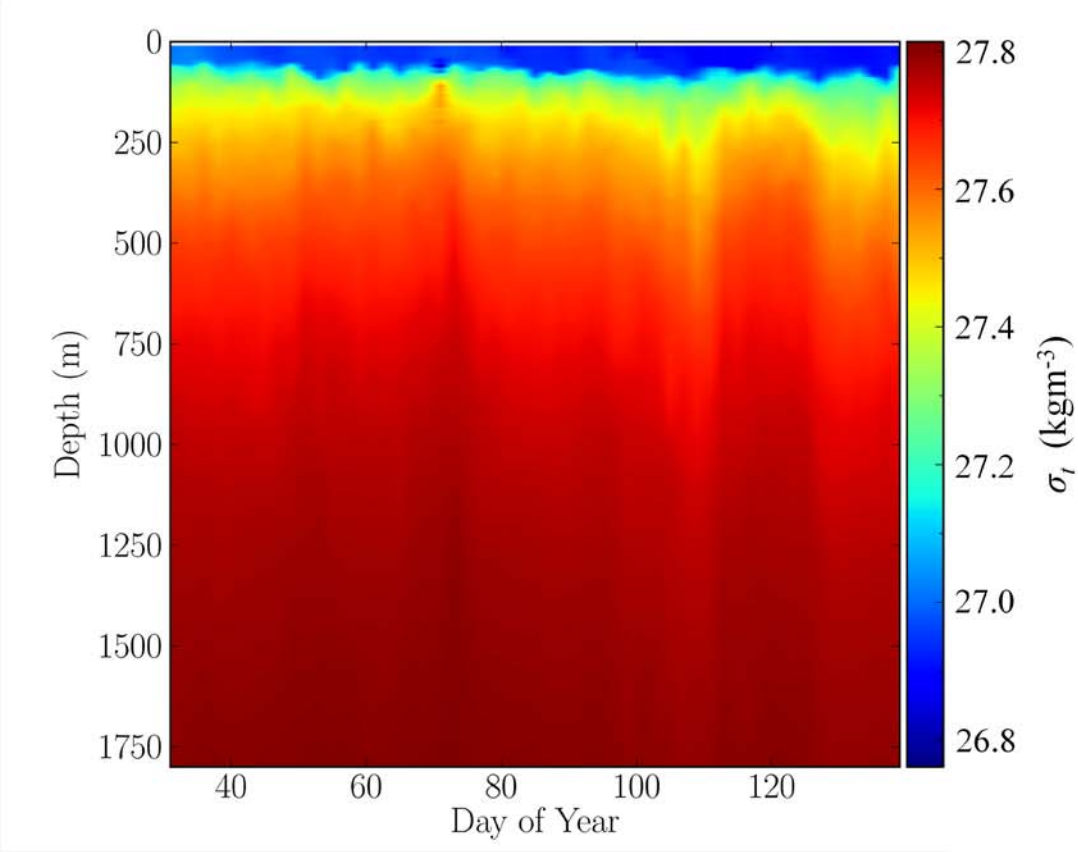

Figure 2.5: Gridded σ_t in kgm^{-3}. Salinity and temperature are measured on the biofloat at sampling depths found in Table (2.1). σ_t = ρ - 1,000 where ρ is calculated at each depth following Equation (2.1) and linearly interpolated to grid from 10 m to 1,800 m depth with a 0.5 m resolution.

$$[\text{CDOM}] = 0.0895(\text{Counts}_{output} - 39) \tag{2.4}$$

As with the flourescnece measurements, the signal output from the backscatterometer was also in "counts." The WETLab calibration sheet provides the conversion from signal output to the total volume scattering function,

$$\beta(\theta) = 1.585\text{E}^{-6}(\text{Counts}_{output} - 47), \tag{2.5}$$

where $\beta(\theta)$ is the total volume scattering function with units m^{-1}sr^{-1}. From Sullivan

et al. (2013), the total volume scattering function is defined as the total radiant intensity ($\mathrm{d}I(\theta)$) scattered by a unit volume ($\mathrm{d}V$) in the direction θ per unit of irradiance (E),

$$\beta(\theta) = \frac{1}{E}\frac{\mathrm{d}I(\theta)}{\mathrm{d}V}. \tag{2.6}$$

To measure scattering by particles in the water column, the total volume scattering function is decomposed into scattering by salt water ($\beta_{sw}(\theta)$) and the particles ($\beta_p(\theta)$) following Boss and Pegau (2001):

$$\beta(\theta) = \beta_{sw}(\theta) + \beta_p(\theta). \tag{2.7}$$

Scattering in a liquid is due to microscopic changes in the refractive index, ni (Einstein, 1910), which results from density and concentration (mixing ratio) fluctuations (Zhang et al., 2009). Therefore, the volume scattering function for salt water is further decomposed into scattering due to density fluctuations ($\beta_{swd} \approx \partial ni/\partial\rho$) and scattering due to concentration fluctuation ($\beta_{swc} \approx \partial ni/\partial S$). Zhang et al. (2009) includes both of these fluctuations in their calculation of the volume scattering function for salt water, and their methodology is implement in this study.

The total backscatter coefficient (m^{-1}) is found by integrating the total volume scattering function in the backward direction over $\pi/2$ to π radians, directly following the methodology of Sullivan et al. (2013):

$$b_b = 2\pi \int_{\pi/2}^{\pi} \sin(\theta)\beta(\theta)d\theta. \tag{2.8}$$

Similar to Equation (2.7), the total backscatter coefficient can be decomposed into contributions from salt in pure water and particles, b_{bsw} and b_{bp}, respectively. A nondimensional conversion factor, $\chi(\theta)$, is introduced to related the volume scattering functions to the backscatter coefficients (Maffione and Dana, 1997). Following Boss and Pegau (2001),

$$
\begin{aligned}
b_b &= 2\pi\beta(\theta)\chi(\theta), \\
b_{bsw} &= 2\pi\beta_{sw}(\theta)\chi_{sw}(\theta), \text{ and} \\
b_{bp} &= 2\pi\beta_p(\theta)\chi_p(\theta).
\end{aligned} \tag{2.9}
$$

Substituting Equation (2.7) into the expression for the particle backscatter coefficient in Equation (2.9) gives:

$$
b_{bp} = 2\pi\chi_p(\theta)\left(\beta(\theta) - \beta_{sw}(\theta)\right). \tag{2.10}
$$

In Equation (2.10), $\beta(\theta)$ is calculated from the raw data output in Equation (2.5) and $\beta_{sw}(\theta)$ is calculated following the methods of Zhang et al. (2009).

The the centroid angle on WETLabs ECO-BB (scattering) instruments is 124^o (Stahlke, 2014). Although this centroid angle was not explicitly cited, Boss and Pegau (2001) found χ_p to be between 1.12 for a centroid angle of 120^o and 1.17 for 130^o. Similarly, for centroid angles of 120^o and 130^o, Sullivan and Twardowski (2009) found χ_p values of 1.097 and 1.153, respectively. However the nondimensional conversion factors must be convoluted with the specific sensor's angular weight function as volume scattering measurements are sensor-specific (Sullivan and Twardowski, 2009; Sullivan et al., 2013; Twardowski, 2014). For the ECO-BB sensor with a centroid angle of 124^o, Sullivan and Twardowski (2009) applied this correction and found 1.076 to be the value for χ_p which is used in this study.

As with profiles of σ_t, temperature, and salinity, the backscatter coefficient, chlorophyll-a concentration and CDOM concentration profiles are linearly interpolated onto a fixed grid. The grid ranges from 10 m to 1800 m depth with a vertical resolution of 0.5 m. The resulting gridded profiles between DOY 31 and 139 are contoured in Figures (2.6) - (2.8). The noisy CDOM signal in Figure (2.8) is likely due to the interpolation errors resulting from the discrete sampling performed by the biofloat

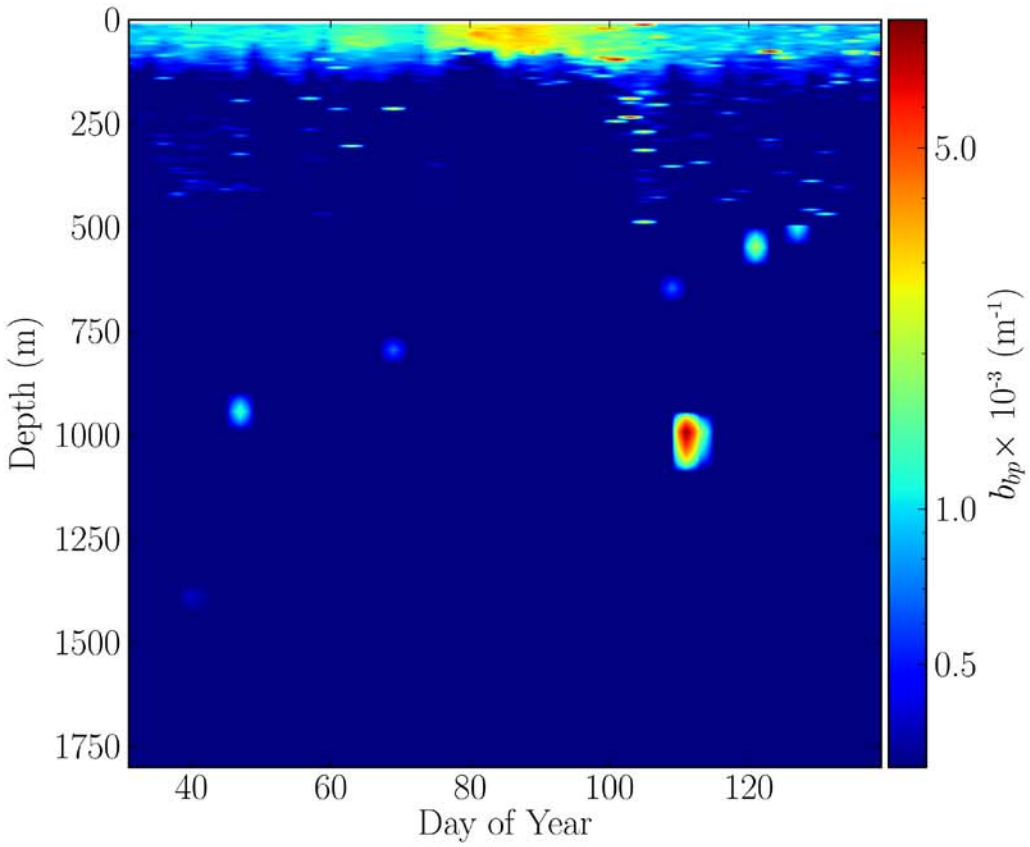

Figure 2.6: Gridded back scatter coefficient values (b_{bp}) with units of m^{-1}. The back scatter coefficient is calculated at sampling depths found in Table (2.1) and linearly interpolated to grid from 10 m to 1,800 m depth with a 0.5 m resolution.

during ascent to the surface.

2.2 OSCAR Surface Currents

The Ocean Surface Current Analysis–Real Time (OSCAR Currents) data product is a collaborative effort between the National Oceanic and Atmospheric (NOAA)/National Environmental Satellite, Data, and Information Service (NESDIS), and Earth and Space Research (ESR) which is a non-profit scientific research institute. The product is freely available online at http://www.oscar.noaa.gov/.

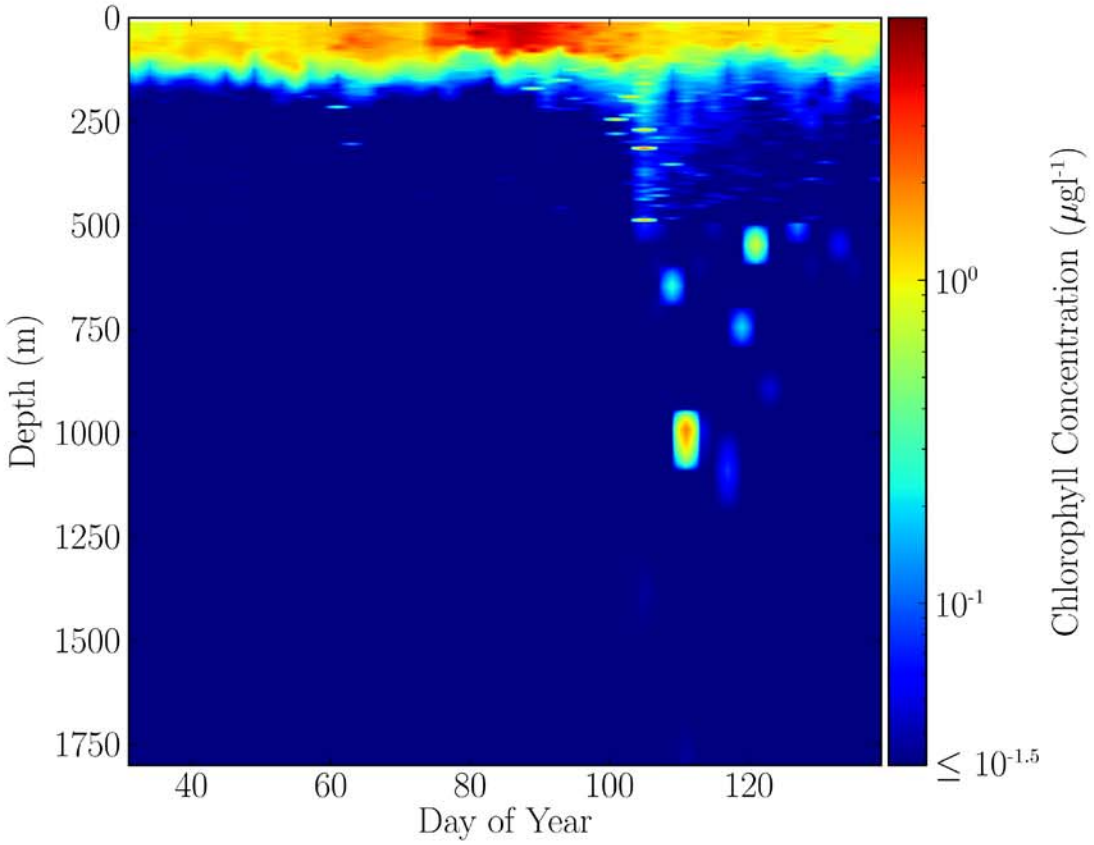

Figure 2.7: Gridded chlorophyll-a concentration (μgl^{-1}). The chlorophyll-a concentration is calculated at the sampling depths found in Table (2.1) and linearly interpolated to grid from 10 m to 1,800 m depth with a 0.5 m resolution.

The currents are computed by combining a quasi-steady geostrophic model with wind-driven ageostrophic currents and thermal wind adjustments. The currents are averaged over the upper 30 m of the ocean. The full model description is available in Bonjean and Lagerloef (2002), thus I will only present an overview of their methodology here. The currents averaged over the upper 30 m of ocean are calculated by:

$$if\overline{\mathbf{U}} \equiv \frac{if}{h}\int_{-h}^{0}\mathbf{U}(z)dz = -g\nabla\zeta + \frac{h}{2}\nabla\theta + \frac{\tau - A\mathbf{U}'(-h)}{h}. \tag{2.11}$$

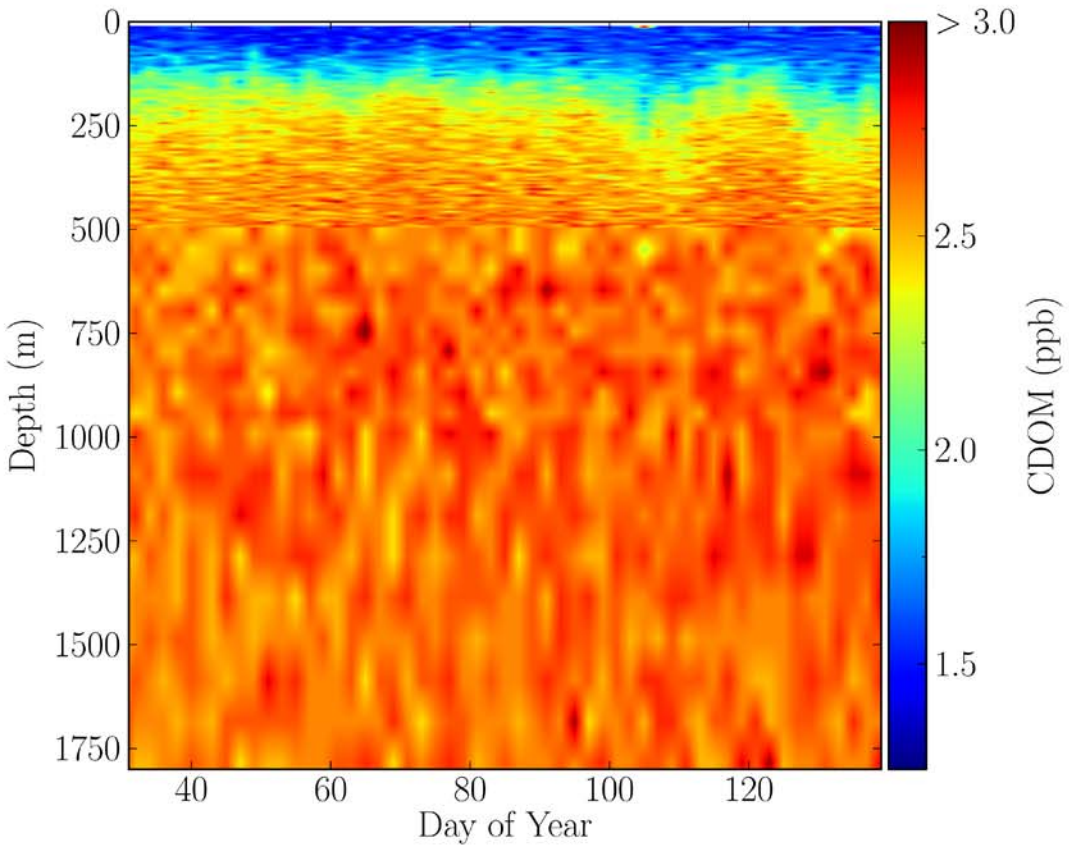

Figure 2.8: Gridded CDOM concentration signal (ppb). The CDOM signal is calculated at that sampling depths found in Table (2.1) and linearly interpolated to grid from 10 m to 1,800 m depth with a 0.5 m resolution.

In Equation (2.11) $\mathbf{U}(x, y, z, t) \equiv u + iv$ is the horizontal velocity vector with the overbar denoting an average velocity to depth h (30 meters) and $\mathbf{U}' \equiv \mathbf{U}_z$ denoting the vertical shear which is assumed to equal τ/A at the ocean surface and zero at a depth $> h$=30 m. $\nabla \equiv \partial/\partial x + i\partial/\partial y$, while the vector wind stress field divided by density is represented by $\tau = \tau^x + i\tau^y$. g is the gravitational constant, ζ denotes the displacement of the ocean-atmosphere interface, θ is a buoyancy force proportional to ∇(Sea Surface Temperature), and A is the depth-uniform eddy viscosity that parameterizes the turbulent vertical mixing (Bonjean and Lagerloef, 2002). The first term on the right hand side in Equation (2.11) represents the pressure gradient force (geostrophy) which

is adjusted by the contribution of the second term, the buoyancy gradient. The last term on the right hand side represents the net drag force applied by the wind stress to the depth of h.

The work of Bonjean and Lagerloef (2002) builds on a previous model by Lagerloef et al. (1999) that assumed the surface currents are based solely on geostrophy and wind stress. Following the methods in Lagerloef et al. (1999), Bonjean and Lagerloef (2002) calculated deviations in the TOPEX/Poseidon altimetery sea level data from the temporal mean. More recently, the operational OSCAR data products are incorporating Jason-1 and Envisat altimetery data. Variational analysis of Special Sensor Microwave Imager (SSM/I) winds by (Atlas et al., 1996) compute the surface winds with the wind stress vectors computed using the drag relationship by Large and Pond (1981). Bonjean and Lagerloef (2002) compute the global satellite sea surface temperature fields following the methodology in Reynolds and Smith (1994).

For validation, Bonjean and Lagerloef (2002) showed the OSCAR currents over the subtropical Pacific agreed with drifter field data from Johnson (2001) in both zonal and meridional directions. The NOAA/OSCAR website has OSCAR current validation with respect to drifters posted, when available. As the time of publication, no validation was available in the Drake Passage region during the observational period.

For this study, the unfiltered $1/3^o$ resolution OSCAR current product is used. The currents are packaged as discrete, temporal blocks of five-day averaged currents. The u (zonal) and v (meridional) OSCAR current components are linearly interpolated in time for a daily OSCAR current product then bi-linearly interpolated on a sphere to biofloat locations. At the biofloat locations, the currents are used to project the likely surface ocean trajectories over the course of two days. Figure (2.9) shows the float (black) and likely tracer (gray) trajectories.

Estimates of the surface mesoscale kinetic energy per unit mass (KE) are,

$$KE = \frac{1}{2}\left(u^2 + v^2\right), \tag{2.12}$$

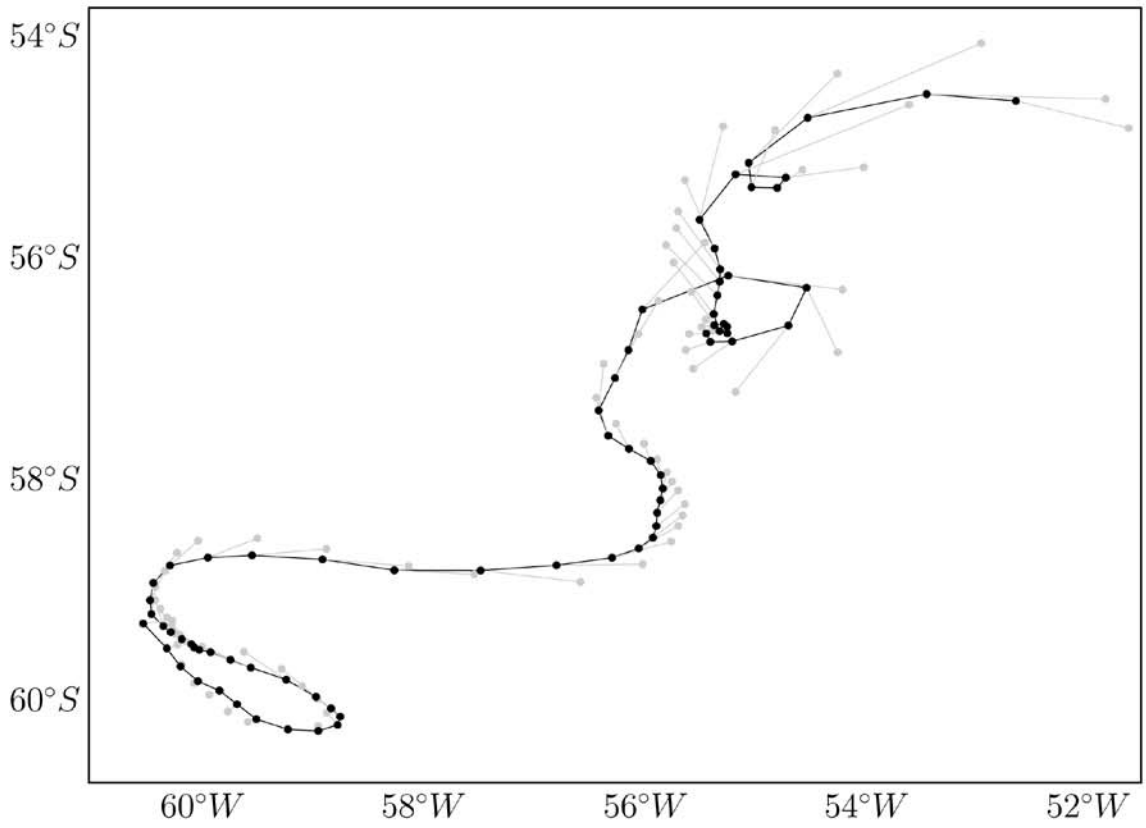

Figure 2.9: A comparison of the float and daily OSCAR surface current tracer trajectories. Black dots show the float surfacing locations between January 10 and June 4, 2013 with black lines connecting the dots. The gray lines and dots show the OSCAR surface current tracer trajectories from each float surfacing location.

where the u and v components of the OSCAR currents. With a one-third degree spatial resolution and a five-day sampling period, the OSCAR currents are well-suited to resolve the mesoscale dynamics in the SO which occur on the order of 100 km spatially and 10 days temporally (Daniault and Menard, 1985).

Chapter 3

INVESTIGATING HIGH MESOSCALE KINETIC ENERGY AS A LIMITING FACTOR FOR PHYTOPLANKTON ABUNDANCE IN DRAKE PASSAGE

3.1 Introduction

The SO is a high latitude ecosystem and classified as a high nitrate, low chlorophyll (HNLC) region. Iron availability is thought to be the primary limiting factor for phytoplankton growth in the SO (Martin, 1990; Martin et al., 1990; Venables and Moore, 2010), and hence the SO has drawn considerable attention as a potential site for augmenting the export of atmospheric CO_2 to the deep ocean through iron fertilization (Smetacek et al., 2012).

While favorable surface ocean iron concentrations are certainly necessary for high phytoplankton abundance in the SO, this study suggests that it is not sufficient. In this chapter, surface ocean mesoscale kinetic energy is investigated as a potential control on phytoplankton abundance, and therefore the biological pump, in the Drake Passage region. To my knowledge, the data presented here are the first observations that show a link between energy containing mesoscale dynamics and the naturally occurring phytoplankton abundance in the HNLC SO.

3.2 Mesoscale Kinetic Energy and Phytoplankton Abundance

For this analysis, five-day surface chlorophyll-a concentration ($[Chl]_{sfc}$) composites were made from the National Aeronautics and Space Administration's (NASA) daily, 9 km, level 3 Moderate Resolution Imaging Spectroradiometer (MODIS)/Aqua chlorophyll-a concentration product. The MODIS/Aqua chlorophyll-a data were subset into the spatial box in Figure (3.1a) that we use to define the Drake Passage region

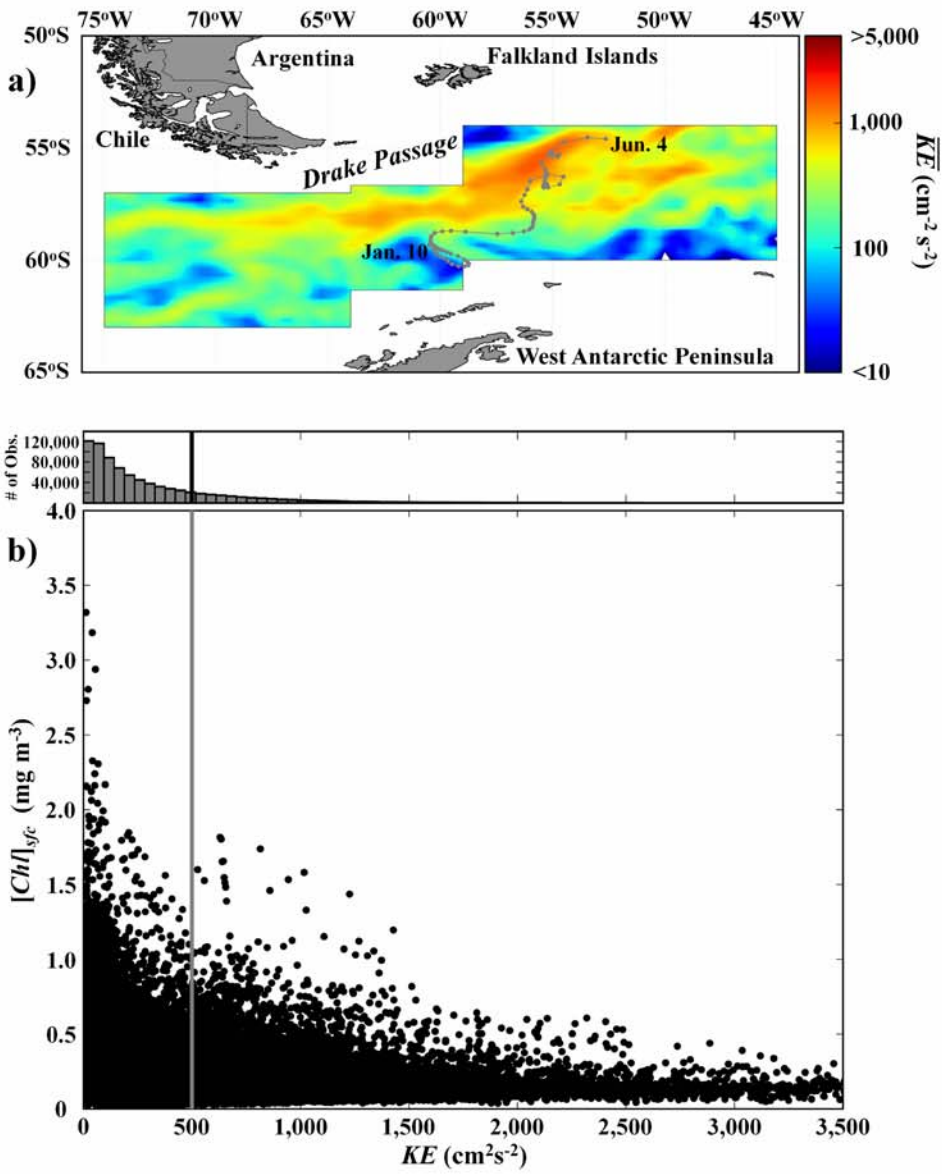

Figure 3.1: *a)* The surface mesoscale kinetic energy per unit mass (KE) averaged across the Drake Passage region (defined as the boxed area) over the observational period ($\overline{KE}$). The biofloat trajectory and surface locations (dots) are in gray. *b)* The MODIS/Aqua five-day composite surface chlorophyll-a concentration ($[Chl]_{sfc}$) plotted with coincident estimates of KE. As detailed in the text of this chapter, the vertical gray line at 500 cm^2 s^{-2} represents the transition point between high and low KE regimes.

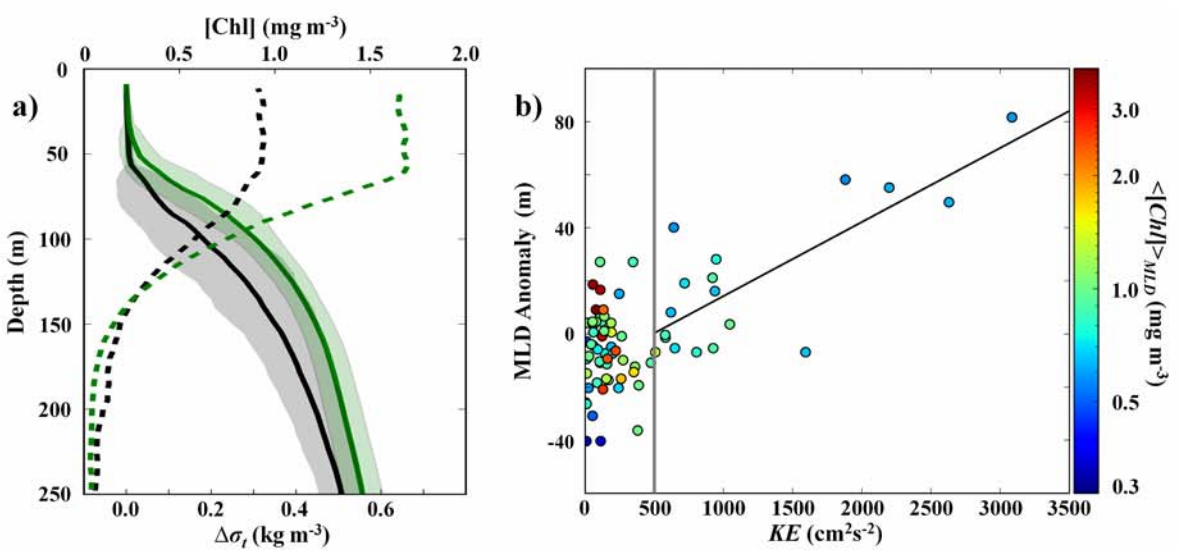

Figure 3.2: *a)* Mean normalized density profiles ($\Delta\sigma_t$) from the biofloat (solid lines) $\pm$ one standard deviation (shading) for high (black) and low (green) levels of surface mesoscale kinetic energy per unit mass (KE) calculated at biofloat locations. The dashed lines denote the mean [Chl] profiles for high (black) and low (green) levels of KE. 500 $\mathrm{cm^2 s^{-2}}$ is the transition between high and low KE. σ_t is the density calculated from only the biofloat temperature and salinity profiles minus 1,000. $\Delta\sigma_t$ is the σ_t value at each depth normalized by the surface σ_t value. *b)* The MLD anomaly in each biofloat profiles plotted against KE and colored by the mean [Chl] above the MLD in each biofloat profile ($<[Chl]>_{MLD}$). Positive anomalies indicate MLD's deeper than in the mean MLD. The black line shows the linear regression (Equation 3.1) between the MLD anomalies and high levels of KE with a statistically significant $\mathrm{R^2} = 0.63$. The linear regression was only performed on observations with KE levels greater than 500 $\mathrm{cm^2 s^{-2}}$, and the corresponding MLD anomalies.

for this study. The $[Chl]_{sfc}$ corresponds with each of the discrete OSCAR currents data blocks. To calculate coincident satellite estimates of KE and $[Chl]_{sfc}$, the discrete, five-day OSCAR current product was bi-linearly interpolated on a sphere to each $[Chl]_{sfc}$ location and the KE at each location was calculated following Equation (2.12).

Figure (3.1b) shows the relationship between $[Chl]_{sfc}$ and the KE across the entire Drake Passage region during the observational period. The analysis shows that high levels of KE correspond with low phytoplankton abundance across the Drake Passage, while high phytoplankton abundance appears to occur only when the KE is low. The vertical line at $500\,\mathrm{cm^2 s^{-2}}$ in Figure (3.1b) represents the transition point between high and low KE regimes defined here as the mean KE in the Drake Passage region during the observational period ($331\,\mathrm{cm^2 s^{-2}}$) plus one standard deviation ($170\,\mathrm{cm^2 s^{-2}}$). The mean KE estimate agrees with values found in the literature (Nowlin et al., 1981; Daniault and Menard, 1985). Figure (3.1a) shows the mean KE in the Drake Passage region during the observational period, while the histogram along the top of the figure shows the corresponding KE distribution. The probability density function shown in the histogram is clearly not Gaussian; if it were, we would expect approximately 15.6% of KE observations would surpass the $500\,\mathrm{cm^2 s^{-2}}$ threshold. Instead, approximately 18% of KE observations are greater than the $500\,\mathrm{cm^2 s^{-2}}$ threshold.

3.3 APEX Float Observations and Results

To validate the satellite KE–$[Chl]_{sfc}$ relationship shown in Figure (3.1b), in-situ observations from the biofloat was analyzed. Figure (3.1a) shows the biofloat trajectory and the individual dots along the track show the biofloat surface positions. The fast, two-day profiling cycle allowed the biofloat to act as a near-Lagrangian tracer with respect to the surface ocean motion. The profiling frequency was able to resolve mesoscale and some sub-mesoscale processes in the surface ocean.

Figure (3.2a) shows mean σ_t profiles from the biofloat, normalized by the surface σ_t value ($\delta\sigma_t$). The profiles are partitioned into high and low KE regimes with $500\,\mathrm{cm^2 s^{-2}}$ as the transition value. In this figure, the KE is calculated from the

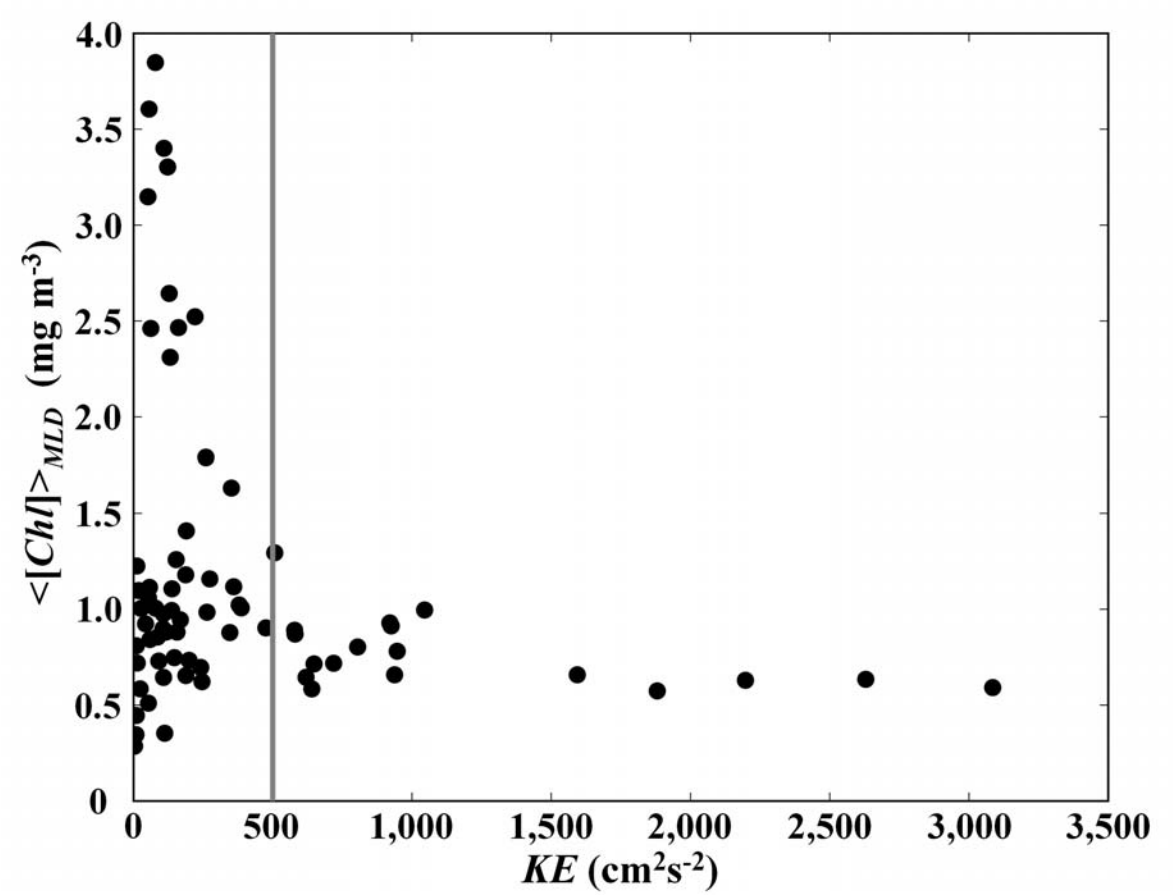

Figure 3.3: The depth averaged chlorophyll-a concentration above the MLD in each biofloat profile ($<Chl>_{MLD}$) plotted against the corresponding daily surface mesoscale kinetic energy per unit mass (KE) at biofloat locations. These in-situ observations from the biofloat match the satellite observation in Figure (3.1b) and suggest low levels of KE are a necessary (but not sufficient) condition for high phytoplankton abundance, while high levels of KE appear to limit phytoplankton abundance in the Drake Passage region.

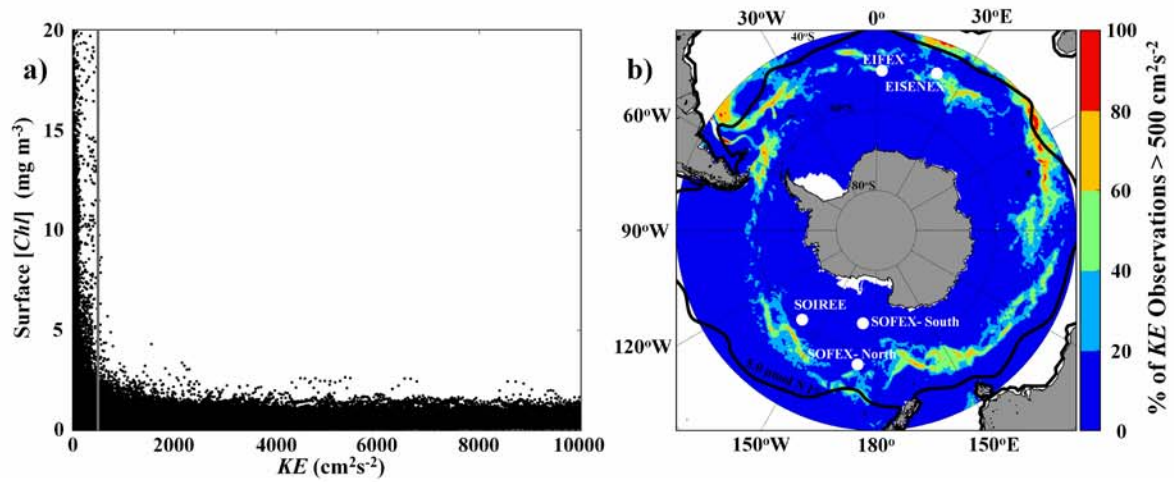

Figure 3.4: *a)* The MODIS/Aqua five-day composite surface chlorophyll-*a* concentration ($[Chl]_{sfc}$) is plotted against coincident estimates of the surface mesoscale kinetic energy per unit mass (KE) for the open water of the SO (south of 45 °S and north 65 °S). This satellite analysis was conducted for the broader austral summer from November 1, 2012 through March 31, 2013. The 500 $cm^2\,s^{-2}$ cut-off between high and low KE used in the analysis of the Drake Passage region is also plotted (gray line). As in the Drake Passage, high levels of KE appear to limit phytoplankton abundance across the open SO. *b)* The percent of OSCAR mesoscale kinetic energy observations greater than 500 $cm^2\,s^{-2}$ in austral summer (December, January, and February) between 2004–2013. The black contour shows the climatological location of the 5 $\mu mol\,l^{-1}$ surface nitrate (N) concentration during austral summer (Garcia et al., 2009). SO locations south of the 5 $\mu mol\,N\,l^{-1}$, and where the percentage of KE observations $> 500\,cm^2\,s^{-2}$ is high, may be unsuitable for large-scale iron additions as a means of enhancing the biological pump. Also shown are the locations of SO iron fertilization experiments: SOIREE (Boyd et al., 2000), EISENEX (Gervais et al., 2002), SOFEX-South and -North (Coale et al., 2004), and EIFEX (Hoffmann et al., 2006).

daily OSCAR currents at each biofloat location. Figure (3.2a) also shows the mean chlorophyll-a concentration profiles ($[Chl]$, a proxy for phytoplankton abundance) which were calculated from the chlorophyll-a fluorescence measurements.

In Figure (3.2a), the biofloat observations show a significant difference between the mean vertical structure of the surface ocean water column (solid lines) above and below $KE = 500\,\mathrm{cm^2 s^{-2}}$. The mixed layer depth (MLD) is defined as as the depth when each $\partial\sigma_t/\partial z$ profile is first greater than $0.0015\,\mathrm{kg\,m^{-4}}$ descending from the surface. The mean MLD from all σ_t profiles was 55 m which agrees with the range of observed MLD's in the Drake Passage region (Dong et al., 2008). The mean MLD for the low KE profiles was 48 m and 74 m for the high KE profiles.

Figure (3.2b) shows that the MLD's in the low KE regime appear to vary about mean MLD without a trend or relationship. In contrast, for profiles with KE levels greater than $500\,\mathrm{cm^2 s^{-2}}$ the MLD's appear at or deeper in the water column than the mean MLD. The KE describes 63% of the variability in the MLD's in the high mesoscale kinetic energy regime ($\mathrm{R}^2 = 0.63$ and $\mathrm{P} < 0.0001$) with the linear regression (black line in Figure 3.2b):

$$\mathrm{MLD}_{pred} = 0.028KE - 13.62. \tag{3.1}$$

This indicates that, on average, when the KE is high, the mesoscale dynamics are sufficiently strong to dictate the vertical structure of the surface ocean water column and deepen the mixed layer. However, when the KE is low, the mesoscale dynamics appear insufficient to impact the vertical structure of the water column.

In response to the difference between the mean high and low KE σ_t profiles, the mean $[Chl]$ profiles in the surface ocean are also different. Figure (3.2a) shows that, on average, the phytoplankton abundance in the surface ocean (dashed lines) is lower during high levels of KE. This is consistent with a deeper mixed layer which potentially decreases phytoplankton residence time in the well-lit euphotic layer (Sverdrup, 1953; Taylor and Ferrari, 2011) leading to light limitation (Falkowski, 1983).

The individual biofloat profiles appear to show that the depth-averaged chlorophyll-*a* concentrations above the MLD ($<[Chl]>_{MLD}$) are low (generally less that $1\,\mathrm{mg\,m^{-3}}$) when the KE is high (Figure 3.2b). However, the $<[Chl]>_{MLD}$ can be high during low levels of KE because, on average, the mesoscale dynamics appear insufficiently strong to change the vertical structure of the water column which potentially alleviates light availability as a limiting factor for phytoplankton growth. Indeed, our coincident estimate of KE and $<[Chl]>_{MLD}$ from the biofloat in Figure (3.3) match the KE–$[Chl]_{sfc}$ relationship observed by satellites (Figure 3.1b).

3.4 Discussion

High phytoplankton abundance was not observed in-situ (Figure 3.3) or from satellite (Figure 3.1b) observations while the KE was high. Biofloat observations appear to reveal that high levels of KE deepen the vertical structure of the water column (Figure 3.2) which could control phytoplankton abundance by decreasing phytoplankton residence time in the well-lit euphotic layer (Falkowski, 1983). Indeed, seasonally driven (Sverdrup, 1953) and turbulence driven (Taylor and Ferrari, 2011) residence time in the euphotic layer can regulate phytoplankton abundance. These observations suggest a mesoscale mechanism for light limitation of naturally occurring phytoplankton abundance in the Drake Passage region. This further implies that low levels of KE may be a necessary, but not sufficient, condition for high phytoplankton abundance, however other limiting factors (i.e. iron availability, grazing) still remain.

Additional in-situ studies featuring either prolonged field work or biofloat deployments will be necessary to confirm this KE–chlorophyll abundance relationship. Validating this mechanism is potentially important because when the scope of the study is broadened to the open waters of the SO, high levels of KE still appear to limit $[Chl]_{sfc}$ (Figure 3.4a). The implication is that there may be regions of the SO that are unlikely to support a phytoplankton blooms because of their frequently high KE, even if other limiting factors such as iron availability are alleviated. Figure (3.4b) shows the percent of KE observations above $500\,\mathrm{cm^2\,s^{-2}}$ during the austral summer

Study	Latitude	Longitude	KE (cm^2s^{-2})	Notes
SOIREE	61.0 S	220.0 E	N/A	The site was chosen in-part due to "low eddy activity" and "low horizontal shear."
EisenEx	48.0 ^{o}S	21.0 ^{o}E	14.1–108.2	The iron injection was inside a mesoscale eddy to ensure "stable hydrographic conditions."
SoFEX South	66.5 ^{o}S	188.2 ^{o}E	17.3–33.7	A coherent patch was present throughout the experiment and slowly grew from 225 km^2 to 2,100 km^2.
SoFEX North	56.2 ^{o}S	188.0 ^{o}E	57.8–462.3	Strong horizontal shear stretched the patch into an "elongated filament" 7 km wide by 340 km long.
EIFEX	50.0 ^{o}S	2.0 ^{o}E	8.9–578.3	The iron injection was inside an eddy to ensure a "relatively stable water mass." Iron injections were on experiment days 0 and 15. The initial iron injection nearly doubled the observed chlorophyll-a concentration inside the eddy. However, the day 15 injection was followed by a plateau or slight dip in the observed chlorophyll-a concentration which is at time when we estimate the KE peaked ($\sim$ experiment day 20).

Table 3.1: Estimated mesoscale kinetic energy during iron fertilization experiments in the Southern Ocean. The surface mesoscale kinetic energy per unit mass (KE) is estimated at the latitude and longitude locations corresponding to each iron fertilization experiment. Shown are the KE ranges estimated over the duration of each experiment. The iron fertilization experiments conducted in the Southern Ocean are SOIREE (Boyd et al., 2000), EisenEx (Gervais et al., 2002), SoFEX South and North (Coale et al., 2004), and EIFEX (Hoffmann et al., 2006). The KE is not available at the SOIREE study location. The experiment site selection criteria for each study is summarized in the notes, along with any supplemental information about the environmental conditions or experiment.

from 2004-2013. Also plotted is the climatological location of the $5\,\mu\mathrm{mol\,l^{-1}}$ surface nitrate (N) concentration contour during austral summer (Garcia et al., 2009) which roughly defines the extent of the SO HNLC region (south of the line). Assuming the analysis in the Drake Passage region is applicable across the open waters of the SO, large regions of the SO may be unsuitable for large-scale iron fertilization experiments because low KE appears to be a conditional control on phytoplankton abundance. For example, large scale iron addition experiments alleviate a major limiting factor on phytoplankton abundance in the SO; however, these experiments (Boyd et al., 2000; Gervais et al., 2002; Coale et al., 2004; Hoffmann et al., 2006; Smetacek et al., 2012) were preferentially conducted in low KE environments (Table 3.1). Therefore it is possible that the general experimental design of iron addition occludes KE as a controlling factor of phytoplankton abundance through light limitation in the SO.

Chapter 4

EXPLORING THE DEVELOPMENT OF A NATURALLY OCCURING PHYTOPLANKTON BLOOM AND CARBON EXPORT IN THE DRAKE PASSAGE

4.1 Introduction

The natural phytoplankton abundance in the open waters of the SO is seasonally light limited (El-Sayed, 1987) and, in austral summer, characterized by intense, patchy phytoplankton blooms within an otherwise unproductive environment (Moore and Abbott, 2000; Arrigo et al., 2008). Artificial iron injection experiments (Boyd et al., 2000; Gervais et al., 2002; Coale et al., 2004; Hoffmann et al., 2006) have shown that the phytoplankton abundance across the SO is limited by insufficient iron concentrations (Martin, 1990; Martin et al., 1990). Therefore, the SO has become a potential site for enhancing the biological pump through iron fertilization which can sequester increasingly high levels of atmospheric CO_2 in the deep ocean (Smetacek et al., 2012).

While Chapter (3) explores the relationship between kinetic energy and phytoplankton abundance within the oceanic mesoscale regime, this chapter investigates the mechanisms driving the formation of a natural phytoplankton bloom in the Drake Passage when the mesoscale high kinetic energy control on phytoplankton abundance is alleviated. Furthermore, this chapter will investigate mechanisms that may have contributed to post-bloom natural carbon export.

4.2 Biofloat Methods and Observations

Figure (4.1) shows the biofloat chlorophyll-a concentration and σ_t observations in the upper 500 m of the water column between DOY 31 and 139. Figures (4.2a) and (4.2b) show the upper ocean biofloat observations of temperature and salinity.

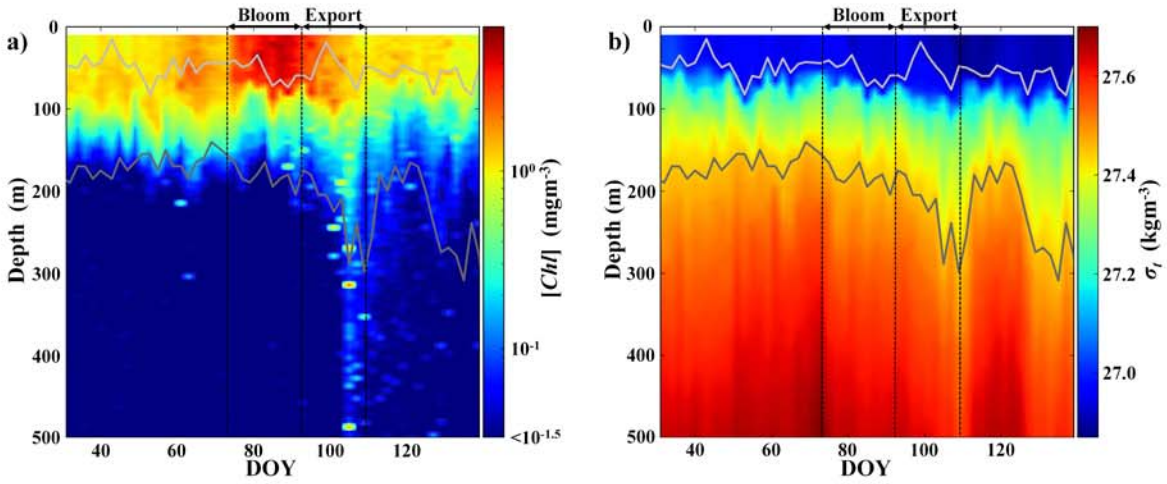

Figure 4.1: *a)* Chlorophyll-*a* concentration ([*Chl*]) and *b)* σ_t observations from 500 m to surface, between DOY 31–139. The biofloat resolved the temporal progression of a naturally occurring phytoplankton bloom and export event (labeled). The mixed layer depth (light gray) and depth of the characteristic isopycnal (z_c, dark gray) are also shown.

Observations of the chlorophyll-*a* concentrations ([*Chl*], a proxy for phytoplankton abundance) and CDOM concentrations (Figure 4.2c) are derived from their respective fluorescence measurements. The particle backscatter coefficient (b_{bp}; Figure 4.2d) is derived from the measured optical backscatter following the Methods Chapter.

The mixed layer depth (MLD) is defined as the depth when each $\partial\sigma_t/\partial z$ biofloat profile is first greater than $0.0015\,\mathrm{kg\,m^{-4}}$ descending from the surface. In addition, $\sigma_t = 27.45\,\mathrm{kg\,m^{-3}}$ is chosen as a reference isopycnal for the upper ocean. The depth of this isopyncal (z_c) approximately tracks the deepest extent of the surface chlorophyll layer (Figure 4.1a) which makes it a reasonable lower bound for depth integrating chlorophyll-*a* concentrations . Furthermore, z_c is within the bottom of the pycnocline and is highly correlated with the depths of surrounding isopycnals (Figure 4.1b) making it suitable for comparing the pycnocline depth between profiles.

The [*Chl*] observations in Figure (4.1a) show the development of a naturally occurring phytoplankton bloom beginning just after DOY 73, followed by an organic

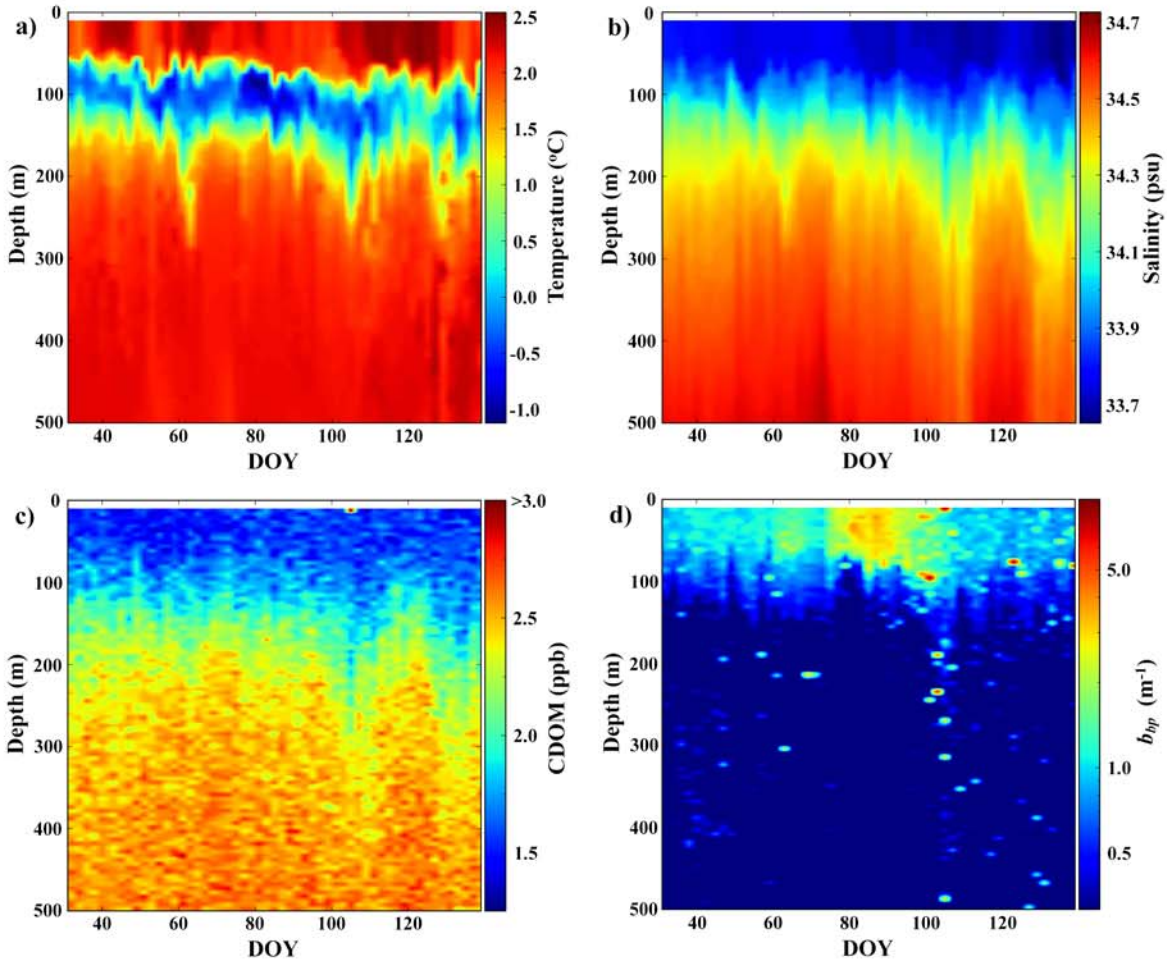

Figure 4.2: Biofloat *a)* temperature, *b)* salinity, *c)* colored dissolved organic matter (CDOM) and *d)* particle backscatter coefficient (b_{bp}) observations from 500 m to the surface between DOY 31 and 139.

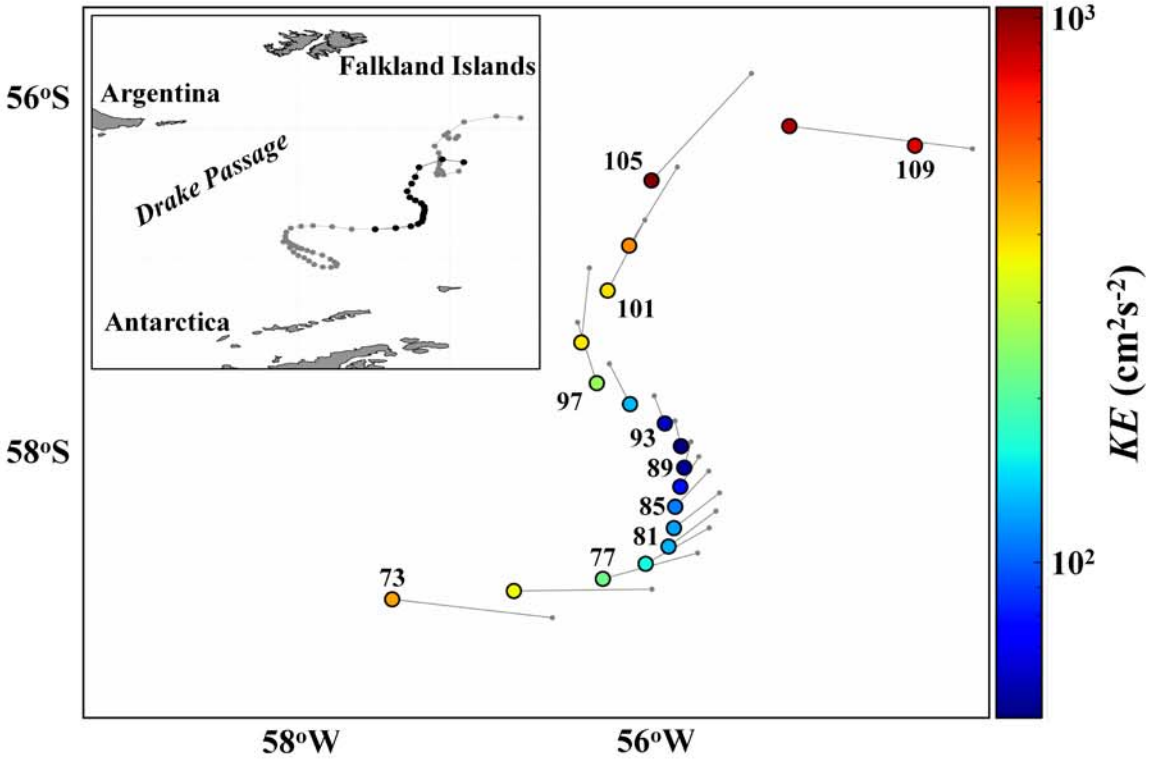

Figure 4.3: Biofloat surfacing locations between DOY 73 and 109 (the bloom-export period). The biofloat locations are colored by the corresponding OSCAR derived mesoscale kinetic energy per unit mass (KE). For each biofloat location, likely surface trajectories over the course of two days (gray line and dots) are derived from daily OSCAR currents (see Methods Chapter). The DOY is labeled next to every other biofloat surface location. The inset shows the biofloat trajectory over the observational period (gray) with the bloom-export period in black and corresponding with the biofloat trajectory in the larger figure.

carbon export event lasting through DOY 109 (the bloom-export period). The fast, two-day profiling cycle allowed the biofloat to capture the surface ocean motion and coherent processes therein, including the temporal progression of the bloom–export event. For validation, the biofloat trajectory during the bloom-export period was compared with likely surface tracer trajectories derived from the National Oceanic and Atmospheric Administration's (NOAA) unfiltered, $1/3^o$ resolution, OSCAR currents. The u (zonal) and v (meridional) OSCAR current components are linearly interpolated in time for a daily OSCAR current product then bi-linearly interpolated on a sphere to biofloat locations where they are used to project the likely surface ocean trajectories over the course of two days. In Figure (4.3), the likely trajectories (gray) show that the Lagrangian biofloat acted as a near-Lagrangian tracer with respect to the surface ocean motion during the bloom-export period.

4.3 Natural Bloom Development

The development of a phytoplankton bloom requires photosynthetic growth to outweigh losses due to respiration, sinking, or grazing. The processes that satisfy this requirement have been studied over a range of spatial and temporal scales for the past century. In the absence of nutrient limitation, the long-standing hypothesis is that a shallow mixed layer depth (MLD) will enhance photosynthetic growth by increasing phytoplankton residence time in the euphotic zone on seasonal- (Sverdrup, 1953) and turbulent-scales (Huisman et al., 1999; Taylor and Ferrari, 2011). In contrast, it has also be suggested that a deepening mixed layer leads to net photosynthetic growth by reducing the interactions between phytoplankton and their grazers through dilution. A deep MLD leads to a de-coupling of the ecosystem which reduces phytoplankton loss via grazing (Behrenfeld, 2010). However, insufficient nutrient availability can also limit phytoplankton growth. The SO is a high nitrate, low chlorophyll region where photosynthetic growth is further limited by surface ocean iron concentrations (Martin, 1990; Martin et al., 1990).

Based on satellite observations (Figure 3.1), low kinetic energy per unit mass (<

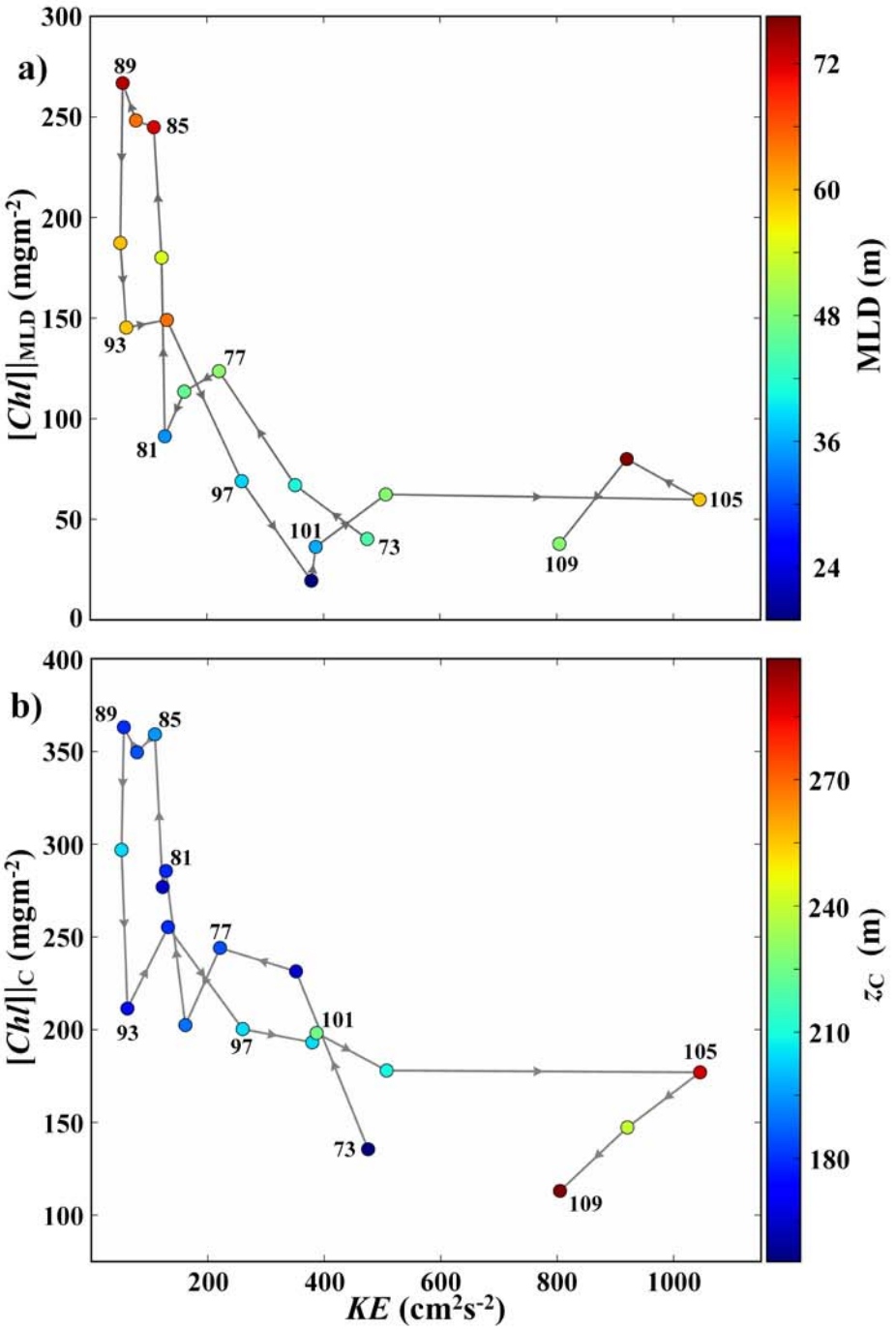

Figure 4.4: *a)* The temporal progression of the *a)* depth integrated chlorophyll-*a* concentration above the MLD ($[Chl]|_{MLD}$) and the *b)* depth integrated chlorophyll-*a* concentration above z_c ($[Chl]|_c$) with respect to the OSCAR surface mesoscale kinetic energy per unit mass (KE). The observations are colored by MLD in *a)* and z_c in *b)*.

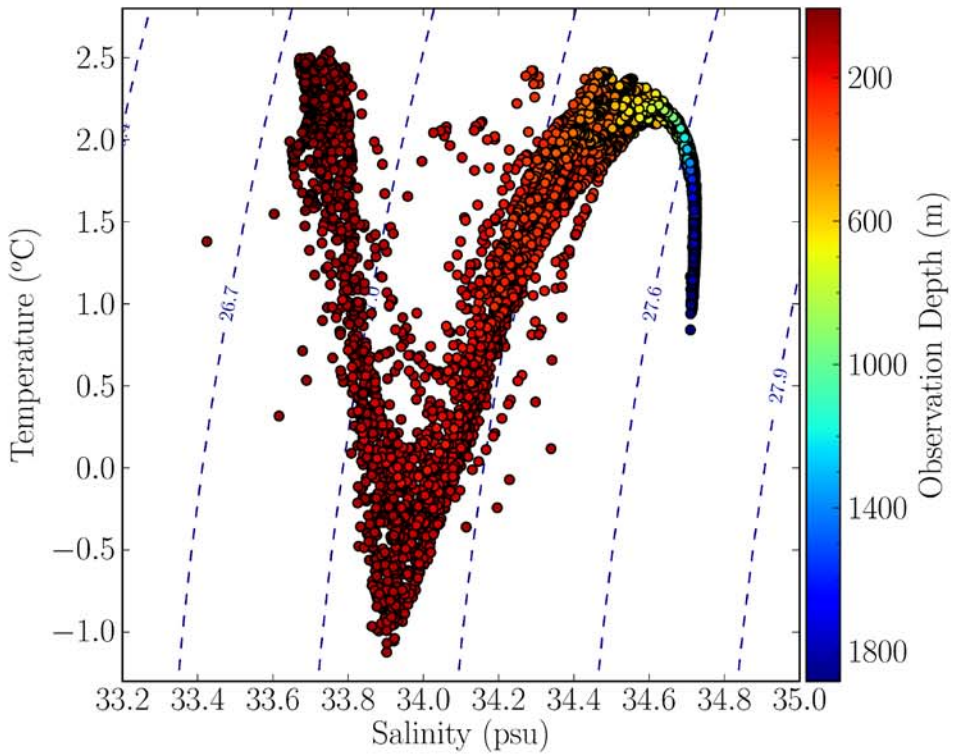

Figure 4.5: Biofloat temperature and salinity observations. The coloring indicates the observation depth. The dashed contouring are values of σ_t - 1000.

500 $cm^2\,s^{-2}$) in the Drake Passage region is a necessary (but not sufficient) condition for naturally high phytoplankton abundance within the oceanic mesoscale regime. The in-situ float observations during the bloom-export period follow this pattern (Figure 4.4). However, relaxing a oceanic mesoscale constraint on high phytoplankton abundance does not explain the cause of the naturally occurring phytoplankton bloom shown Figure (4.1a). This chapter examines the evidence for bloom formation that potentially includes the relaxation of grazing pressure and natural iron deposition.

4.3.1 Evidence for Bloom Formation Via Grazing Relaxation

Figure (4.4) shows the temporal progression of the naturally occurring phytoplankton bloom as it related to the MLD and the the surface ocean mesoscale kinetic

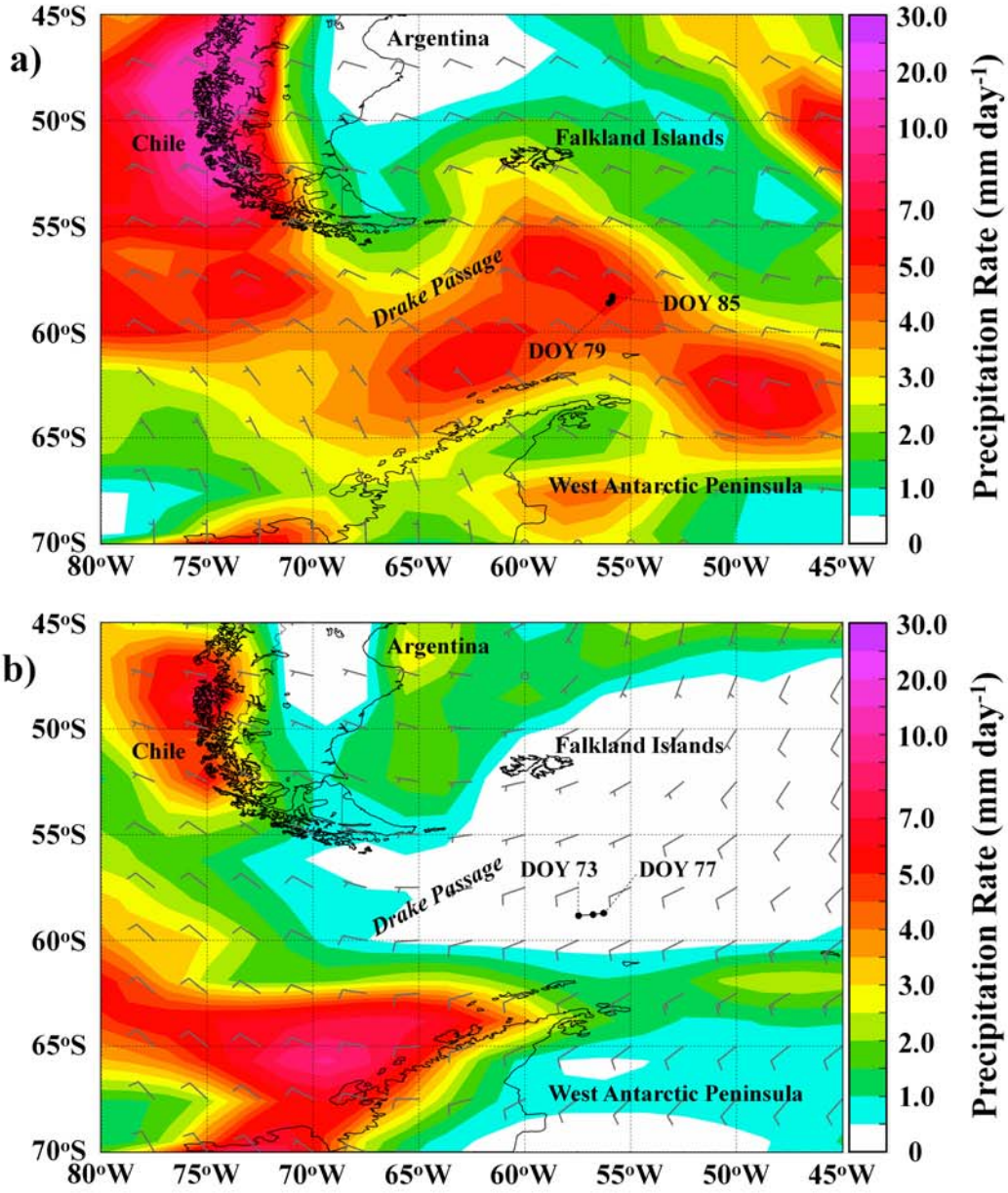

Figure 4.6: NOAA National Center for Environmental Prediction Reanalysis (Kalnay et al., 1996) mean surface precipitation rate and 935 mb winds (barbs) for *a)* DOY 78–86 and *b)* DOY 71–78.

energy. The KE experienced by the biofloat at each surface location is shown in Figure (4.3).

Figure (4.4a) shows the integrated $[Chl]$ above the MLD ($[Chl]|_{MLD}$) in each biofloat profile. On DOY 73, the $[Chl]|_{MLD}$ was $40\,\mathrm{mg\,m^{-2}}$, which compares with the mean $[Chl]|_{MLD}$ ($65\,\mathrm{mg\,m^{-2}}$) measured during the biofloat observational period. Between DOY 73 and the peak $[Chl]|_{MLD}$ observation on DOY 89 (the bloom development period), the $[Chl]|_{MLD}$ increased over six-fold to a value of $267\,\mathrm{mg\,m^{-2}}$, while the MLD deepened by 30 m. The largest deepening of the MLD during the bloom development period was 20 m, and occurred between DOY 81 and 83. This timing corresponded with the highest net $[Chl]|_{MLD}$ growth rate during the bloom development period ($0.34\,\mathrm{day^{-1}}$). The net $[Chl]|_{MLD}$ growth rate between subsequent profiles ($\Delta t = t_1 - t_0$) is estimated by (Behrenfeld, 2010):

$$r = \frac{\ln\left([Chl]|_{MLD_1}\right) - \ln\left([Chl]|_{MLD_0}\right)}{\Delta t}. \tag{4.1}$$

The estimated mean net $[Chl]|_{MLD}$ growth rate during the bloom development period was $0.12\,\mathrm{day^{-1}}$, which is within the observed ranges (Boyd et al., 2000). This suggests a potential a sub-mesoscale analog to ecosystem de-coupling by deepening the mixed layer (Behrenfeld and Boss, 2014); this process could potentially reduce grazing pressure by limiting phytoplankton–grazer interactions which may have contributed to the naturally occurring phytoplankton bloom development. While this observation appears to directly contradict the analysis in Chapter (3), the ecosystem decoupling event observed in this chapter primarily unfolds over a four day period (between DOY 81 and 85) which is different than the scales discussed in the previous chapter. The four day temporal progression is a sub-mesoscale process; mesoscale processes in the SO occur on 10 day temporal scales (Daniault and Menard, 1985).

4.3.2 Evidence for Bloom Formation via Iron Deposition

Surface iron concentrations are a limiting factor for phytoplankton blooms across the SO (Venables and Moore, 2010), including within the Drake Passage (Hoffmann

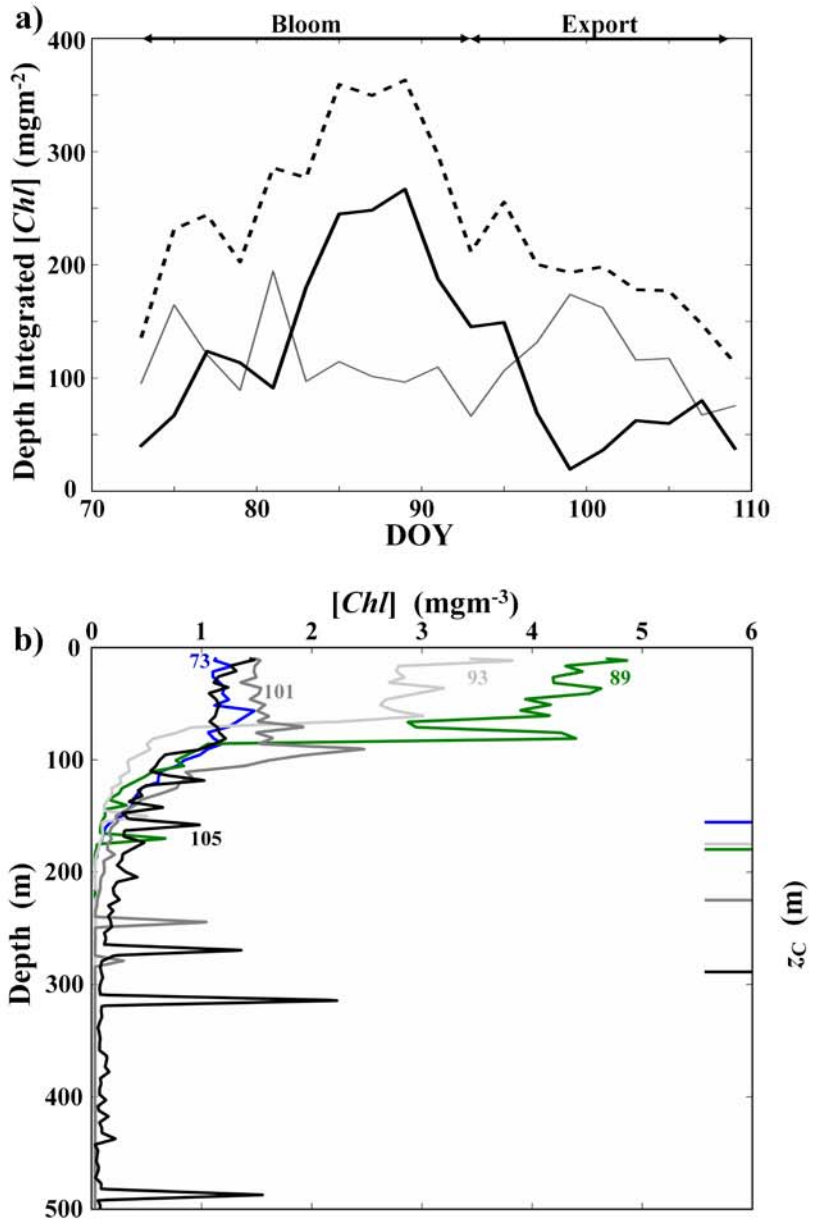

Figure 4.7: *a)* The time series of the depth integrated chlorophyll-a concentration above the mixed layer depth (MLD; solid black), depth integrated chlorophyll-a concentration above the depth of the characteristic isopycnal (z_c; dashed black), and different between to two (gray). The bloom and export periods are labeled. *b)* Chlorophyll-a concentration ($[Chl]$) profiles on days during the bloom-export period selected to shown the temporal progression of the naturally occurring phytoplankton bloom and organic carbon export event. The profile colors match the DOY label colors. The horizontal marks on the right, vertical axis show z_c corresponding to each $[Chl]$ profile (coordinating colors).

et al., 2006). The observed surface iron concentrations in the Drake Passage are low, and generally range 0.1–0.2 nmol Fe l^{-1} (Martin et al., 1990; Klunder et al., 2014). While the biofloat had no means of measuring the surface iron concentration in-situ, the iron concentration required to achieve the observed bloom are estimated by applying known carbon-to-chlorophyll (Hoffmann et al., 2006) and carbon-to-iron ratios (Twining et al., 2004) in the SO. The maximum depth averaged $[Chl]$ above the MLD ($<[Chl]>_{MLD}$) during the bloom development period was chosen for this analysis which will give an upper-bound estimate for the required amount of dissolved iron:

$$\frac{3.8\,\mu\text{g Chl}}{\text{l}} \times \frac{25\,\text{g C}}{1\,\text{g Chl}} \times \frac{1\,\text{mol C}}{12\,\text{g C}} \times \frac{45\,\mu\text{mol Fe}}{1\text{mol C}} \approx 0.36\,\frac{\text{nmol Fe}}{\text{l}}. \tag{4.2}$$

For this estimate, the carbon-to-chlorophyll ratio of 25 g C to 1 g Chl from Figure (5b) in Hoffmann et al. (2006) was used. This value appropriately represents the measured ratios for the largest eukaryotic cells analyzed, just after iron fertilization. The carbon-to-iron ratio is taken at 45 μmol Fe to 1 mol C (Twining et al., 2004) and reflects the measured ratios for diatoms. The maximum $<[Chl]>_{MLD}$ used for Equation (4.2) was 3.8 mg m^{-3} and occurred on DOY 87. Using Equation (4.2), the mean dissolved iron concentration required to maintain the phytoplankton abundance above the MLD during the bloom development period was estimated to be 0.25 nmol Fe l^{-1}, which is also above what is commonly available in the surface waters of the Drake Passage. In fact, the mean dissolved iron concentration required to maintain the observed phytoplankton abundance throughout the full observational period was estimated to be 0.11 nmol Fe l^{-1} which compares favorably with observed surface ocean iron concentration in the Drake Passage (Martin et al., 1990; Klunder et al., 2014).

The upper-bound estimate suggests the naturally occurring phytoplankton bloom would have required approximately doubled the dissolve iron concentrations typically available in the surface waters of this region of the Drake Passage. Therefore, an iron source foreign to the surface ocean may have spurred the formation of the naturally occurring phytoplankton bloom.

A potential source a iron to the surface waters is a mechanical injection from below the ferrouscline (a region of rapidly increasing iron concentrations with depth), observed between 400 and 500 m in the Drake Passage (Martin et al., 1990; Klunder et al., 2014) and deeper than the observed MLDs during the bloom period (Figure 4.1b). Satellite observations show that the surface ocean chlorophyll-a concentrations during austral summer are patchy, but seasonally high along the Polar Front (PF) and within the Antarctic Circumpolar Current (ACC) (Moore and Abbott, 2002). It is well-known that regions of consistently high chlorophyll-a concentrations within the Drake Passage leg of the ACC are associated with bathymetric features in the area (Nolting et al., 1991; Comiso et al., 1993; Moore et al., 1999; Moore and Abbott, 2000, 2002; Holm-Hansen et al., 2005; Sokolov and Rintoul, 2007). Sokolov and Rintoul (2007) showed that regions of high surface ocean chlorophyll-a concentrations along the PF in the Drake Passage are associated with the interaction between the ACC and large-scale topographic features that drive upwelling of micro- and macronutrients. Sokolov and Rintoul (2007) further solidified the argument by showing that the western edge of chlorophyll-a blooms within the Drake Passage leg of the ACC are associated with topographically forced upwelling regions, with blooms persisting along streamlines downstream. However, in the days and weeks leading-up to the bloom, the biofloat trajectory did not encounter any bathymetric features capable of spurring significant vertical transport of micronutrients into the surface ocean, nor are there any large-scale bathymetric features associated with the western edge of the observed bloom. Hence, topographically forced injection of iron from below the deep ferrouscline can be safely rule-out.

The mean position of the PF front is defined by Orsi et al. (1995) as the northernmost extent of the 2 ^{o}C isotherm at 200 m. The 2 ^{o}C isotherm is associated with sub-surface, cold waters between 100 and 200 m where water temperatures are typically observed between -2 and 2 ^{o}C. The cold, sub-surface water is a remnant winter water mass (WW) that sinks below the slightly warmer and fresher surface waters south of the PF. At the PF (a region of surface convergence), the WW mixes with the

sub-Antarctic surface waters north of the PF, with a lingering (but weak) cold signature sinking below 200 m north of the PF (by continuity, convergence at the surface drives downward motion, all else being equal). The persistent WW signature between 100 and 200 m (Figure 4.2a) suggests that the biofloat never crossed the instantaneous position of the PF during the observational period. Furthermore, the temperature-salinity diagram in Figure (4.5) matches previous observations of waters just south of the PF, and within the Antarctic Zone (Gordon et al., 1977). Furthermore, the coherent and uniform structure of the temperature-salinity diagram in Figure (4.5) suggests the biofloat remained in the same water mass throughout the observation period; this further supports the claim that the biofloat was not randomly sampling the region or crossing water masses

It is significant that the biofloat remained south of the PF; Thompson and Gille (2007) showed that in the Drake Passage waters the south of the front, mixing is weak relative to north of the PF. South of the PF the surface ocean is, on average, more susceptible to a double-diffusive convection regime, while north of the PF mixing is, on average, stronger and likely resulting from wind forcing, eddies, near-inertial waves, and internal waves (Thompson and Gille, 2007). Hence, injection due to a mesoscale mixing event seems unlikely, particularly when considering the extremely low KE values observed during the bloom period (Figure 4.3).

Another possible foreign iron source is atmospheric wet iron deposition. Klunder et al. (2014) suggest that patchy areas of increased dissolved iron in the Drake Passage region may be the result of foreign iron deposition from a precipitation event with air mass origins over the South American continent. Figure (4.6a) shows the NOAA/National Center for Environmental Prediction (NCEP) Reanalysis (Kalnay et al., 1996) mean 925 mb winds and precipitation rates in the Drake Passage spanning DOY 78 to 86, just prior to the peak of the bloom. In Figure (4.6a), the mean winds over the Drake Passage between were 10 and 15 $\mathrm{m\,s^{-1}}$ and off the South American continent, while the mean precipitation rates were 5–6 $\mathrm{mm\,day^{-1}}$. In contrast, the previous period from DOY 71 to 78 (Figure 4.6b) featured zonal winds across the Drake

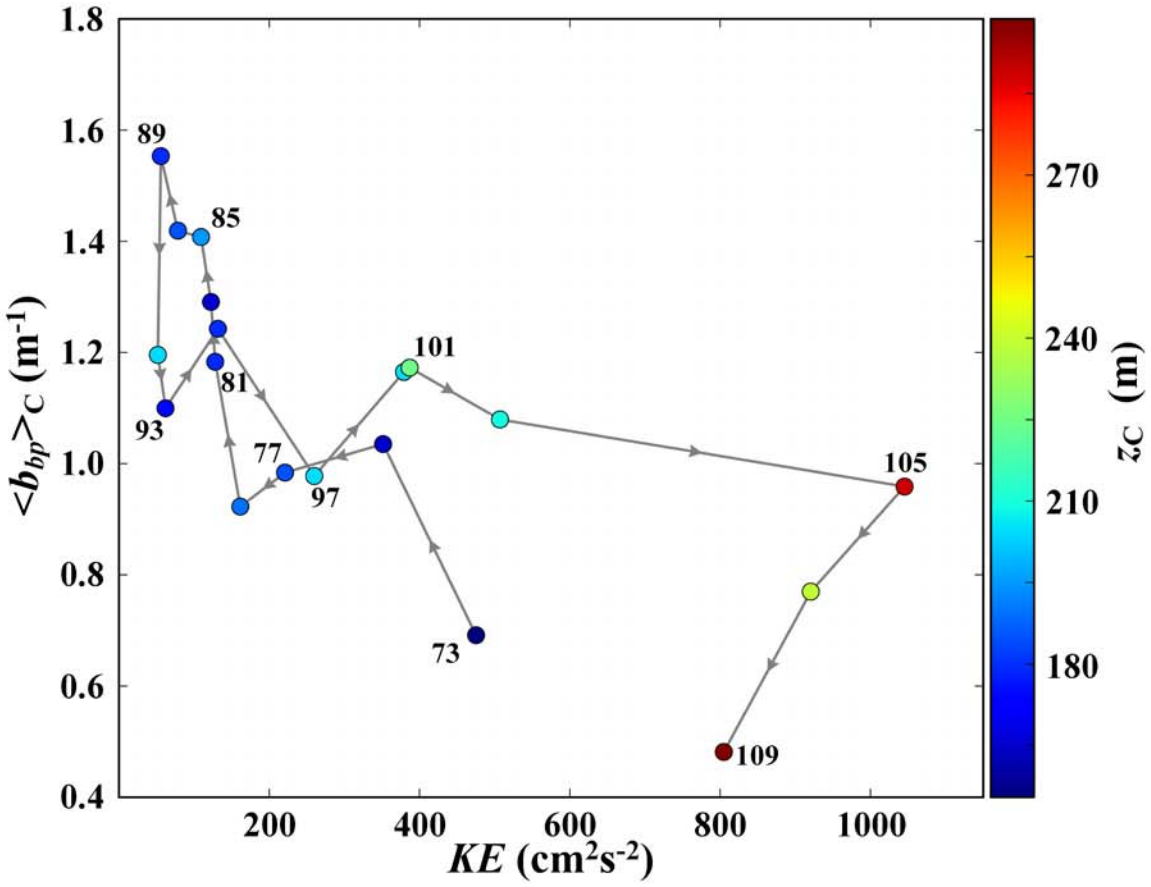

Figure 4.8: The temporal progression of the average particle backscattering coefficient above z_c ($< b_{bpc} >$) with respect to the OSCAR surface mesoscale kinetic energy per unit mass (KE). The observations are colored by z_c.

Passage and no rainfall over the biofloat locations.

Furthermore, the HYbrid Single-Particle Lagrangian Integrated Trajectory (HYSPLIT) three day backward trajectories show that the air at the surface, 1500 m ($\approx$ 850 mb), and 3000 m ($\approx$ 700 mb) above the biofloat locations originates from the South American continent in the days preceding DOY 79 and 81; the highest measured $[Chl]|_{MLD}$ occurred after DOY 81. The period spanning DOY 79 to 81 is coincident with two passing synoptic-scale weather events (shown in the satellite observed fractional cloud cover on the NASA/Giovanni web portal). Therefore, this analysis

suggests that the observed phytoplankton bloom may have been naturally aided by the wet deposition of foreign iron.

Despite the limiting influence of cold water on phytoplankton growth rates (Eppley, 1972), between the beginning of the assumed wet deposition period on DOY 79 and the peak bloom on DOY 89, the $[Chl]|_{MLD}$ increased by 2.5-fold. The increase in $[Chl]|_{MLD}$ over this ten day period, along with the estimated mean growth rate of $0.12\,\mathrm{day}^{-1}$, compares favorably to the biological response to iron fertilization during the Southern Ocean iron-release experiment (SOIREE). During SOIREE, the integrated chlorophyll increased by six-fold within ten days of initial iron injection, with the growth rate increasing to $0.19\,\mathrm{day}^{-1}$ (Boyd et al., 2000). The increase in chlorophyll-*a* during SOIREE may have out-paced the observed increase in $[Chl]|_{MLD}$ from the biofloat due to multiple iron injections throughout the experiment, although there is no way to compare the total iron injection. Nevertheless, the similarities between SORIEE and biofloat observations further support the suggestion that the naturally occurring bloom may have developed due to wet iron deposition from the atmosphere.

4.3.3 Ecosystem Re-coupling and Grazing

After the peak bloom on DOY 89, Figure (4.4) shows a significant loss in depth integrated $[Chl]$ in the surface ocean through DOY 93. Vertical $[Chl]$ profiles in Figure (4.7b) indicate that the loss in surface ocean phytoplankton abundance is uniform with depth. Indeed the $[Chl]|_c$ decreased by 46% during this period while the $[Chl]|_{MLD}$ decreased by 40%. The depth average b_{bp} measurements above the z_c ($< b_{bp} >$) in Figure (4.8) show a similar pattern with a sharp decline in signal between DOY 89 and 93 as observed the $[Chl]|_c$ signal (Figure 4.4b). This is interpreted to indicate that the loss in surface ocean $[Chl]$ over this span was not due to changes in intracellular pigment concentrations. Furthermore, Figure (4.1a) shows that the loss in surface ocean $[Chl]$ was not due to organic carbon export during between DOY 89 and 93.

Figure (4.4a) shows a slight shallowing of the MLD between DOY 89 and 93 while the KE was below $100\,\mathrm{cm}^2\,\mathrm{s}^{-2}$ and likely not a major control on the system. The

interpretation is that the shallowing MLD may have allowed grazers to organize around the concentrated phytoplankton bloom, which is a sub-mesoscale analog to ecosystem re-coupling.

4.4 Organic Carbon Export

Our observations suggest that bloom development is predicated on an injection of iron into the surface ocean, along with ecosystem decoupling that may have lead to grazing relaxation coherent with the peak bloom. Both of these processes occurred during a period of low KE, when presumably the mesoscale processes were insufficiently strong to be a dominate physical feature driving the system Thompson and Gille (2007). However, the mechanisms driving organic carbon export appear different.

Between DOY 93 and 105, the $[Chl]|_c$ remained fairly constant with a decrease of only 16% (Figure 4.4b), while the KE increased by over an order of magnitude from $62\,\mathrm{cm^2\,s^{-2}}$ to $1{,}045\,\mathrm{cm^2\,s^{-2}}$ and z_c deepened from 175 to 289 m. The observations suggest that when the KE rose above $500\,\mathrm{cm^2\,s^{-2}}$ the vertical structure of the water column deepened significantly (Figure 4.9). This suggests that the post-grazed phytoplankton bloom is being diluted as z_c deepens (Figure 4.4b).

Although the $[Chl]|_{MLD}$ decreased by 59% between DOY 93 and 105, the phytoplankton abundance from above the MLD accumulated in the layer between z_c and the MLD (Figure 4.7b). The $[Chl]$ profile on DOY 101 in Figure (4.7a) shows a localized sub-surface $[Chl]$ maxima around 100 m with lower phytoplankton abundance shallower in the water column. This suggests that the post-grazed bloom slowly senesced, aggregated, and began to sink (Figure 4.7a). These processes may have been aided by subduction due to a change in surface ocean stratification. Following iron injection during the Sothern Ocean Iron Experiement (SOFeX), Bishop et al. (2004) showed that surface stratification subducted the surface bloom which isolated the phytoplankton from solar irradiance and the artificial iron course at the ocean surface. Figure (4.2) shows a slightly warmer and fresher surface layer developed post-bloom between DOY 93 and the peak export on DOY 105. If the source of foreign iron was, indeed,

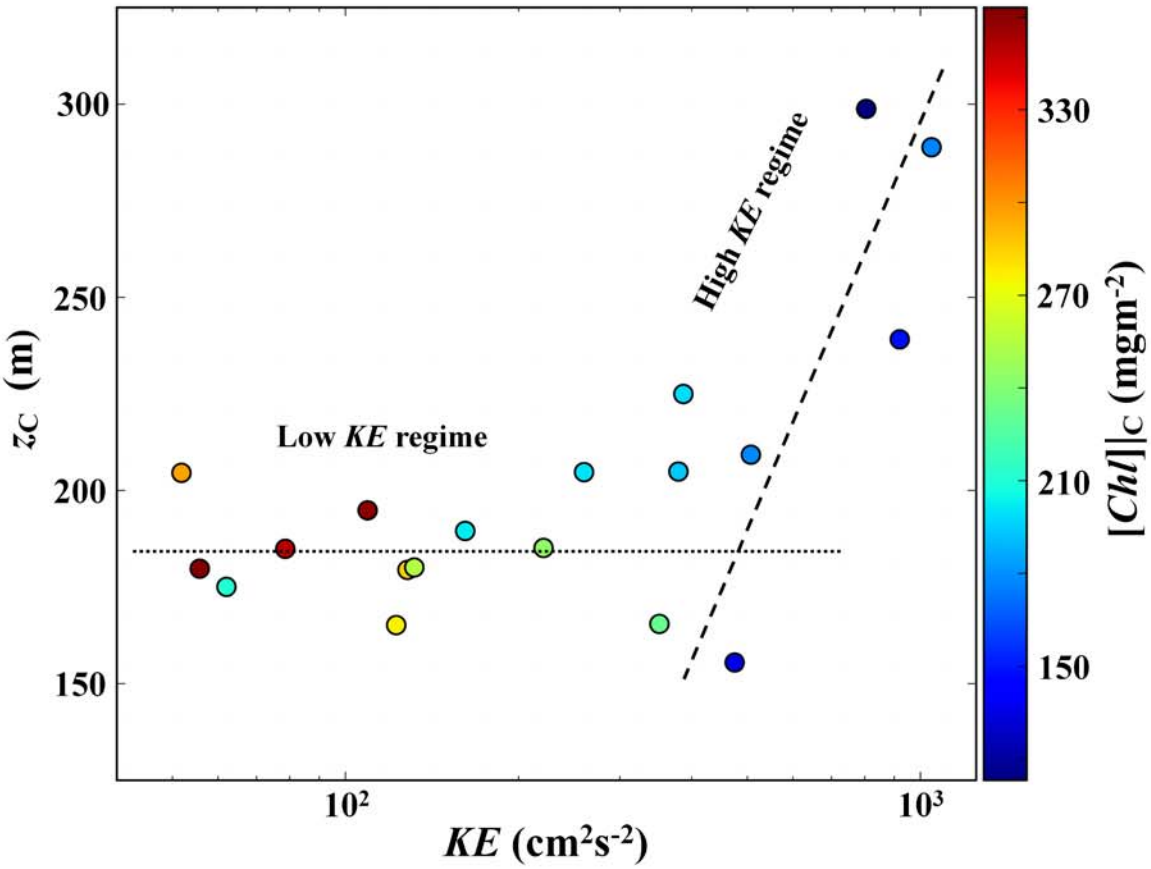

Figure 4.9: The relationship between the depth of the characteristic isopycnal (z_c) and the OSCAR surface mesoscale kinetic energy per unit mass (KE). When KE was above $500\,\mathrm{cm^2\,s^{-2}}$ during the bloom-export period (High KE regime identified in Chapter 3), it appeared strong enough to impact the vertical structure of the water column and deepen z_c.

wet deposition from the atmosphere at the surface, this parallels the artificial injection during SOFeX. Hence subduction of the bloom may have limited available irrandiance while also isolating the bloom from the surface iron supply.

Phytoplankton export to the deep ocean occurred between DOY 101 and 109 as the KE increased and z_c continued to deepen (Figure 4.4b). Deep $[Chl]$ spikes in Figure (4.1b) coincide with spikes in b_{bp} in Figure (4.2d). This indicates these $[Chl]$ features are associated with aggregated phytoplankton (Briggs et al., 2011) that rapidly sink out of the surface ocean (Turner, 2002). The $[Chl]$ profile on DOY 105 in Figure (4.7b) shows the deep $[Chl]$ spikes associated with the naturally occurring organic carbon export.

Given that aggregated phytoplankton sink until reaching their neutral density points, bloom subduction and the KE-driven deepening of z_c (and the surrounding isopycnals) likely played a role in the deeper surface ocean $[Chl]$ signal beyond DOY 83. Under high KE levels, cell aggregates of a particular density are deeper in the water column than expected under a lower KE regime. While a deeper starting point alone is not a sufficient condition for carbon export, the observations appear to suggest that this occurrence primed the system for deep ocean particle export as the neutral density point of the aggregated cells are naturally lower in the water column.

The sinking rate is estimated to be $125\,\mathrm{m\,day^{-1}}$ between DOY 103 and 105 (the timing of the peak export), which is comparable with other particle flux studies (Fischer and Karakas, 2009). Sinking rate estimates are derived from mean changes in the deepest extent of twenty evenly spaced iso-chlorophyll lines ranging 0.1 to $0.4\,\mathrm{mg\,m^{-3}}$.

4.5 Conclusions

An APEX biofloat profiling the Drake Passage water column every two days resolved the development of a naturally occurring phytoplankton bloom and the mechanisms that may lead to an organic carbon export event. The analysis shows that when the low KE precondition is met, the formation of a natural phytoplankton bloom is likely the result of a combination of grazing relaxation through mixed layer deepening

and natural iron deposition for the atmosphere. After the peak bloom, the observations suggest a period of grazering decreased the surface ocean phytoplankton abundance as the MLD shallowed and the ecosystem re-coupled. This analysis further infers that bloom subduction and the *KE*-driven deepening of isopycnals (and the neutral density points of cell aggregates) may be important for natural organic carbon export into the deep ocean.

Chapter 5

SUMMARY

In summary, an APEX biofloat was deployed in the the energetic Drake Passage from January 10 and June 4, 2013 as part of the MUltisensor STability And CHlorophyll Experiment (MUSTACHE). The goal of MUSTACHE was to investigate the mechanisms controlling the formation of naturally occurring phytoplankton blooms in the Southern Ocean. Surface ocean iron concentrations are insufficient in the Southern Ocean and have been shown to limit the natural phytoplankton abundance (and hence the biological pump). Therefore, the Southern Ocean is a potential site for geoengineered atmospheric carbon drawdown through iron fertilization.

The satellite analysis in this study suggests that phytoplankton abundance in the Drake Passage is limited by high levels of surface ocean mesoscale kinetic energy. In-situ observations from the biofloat appear to show that when the mesoscale kinetic energy is high, it is sufficiently strong to deepen the mixed layer which can control phytoplankton abundance by decreasing phytoplankton residence time in the well-lit euphotic layer. Additional satellite observations suggest that the high mesoscale kinetic energy control on phytoplankton abundance in the Drake Passage may be exportable to the open waters of the Southern Ocean.

Furthermore, this study indicates that when the low mesoscale kinetic energy pre-condition is satisfied, the mechanisms important for natural bloom formation in the Drake Passage are grazing relaxation and foreign iron deposition. Following the bloom, the analysis in this study suggests that high levels of mesoscale kinetic energy facilitated organic carbon export into the deep ocean by deepening isopycnals in the surface ocean, and hence the neutral density points phytoplankton aggregates.

BIBLIOGRAPHY

Arrigo, K. R., van Dijken, G. L., and Bushinsky, S. (2008), 'Primary production in the Southern Ocean, 1997-2006', *Journal of Geophysical Research: Oceans* **113**(C8).

Atlas, R., Hoffman, R. N., Bloom, S. C., Jusem, J. C. and Ardizzone, J. (1996), 'A multiyear global surface wind velocity dataset using SSM/I wind observations', *Bull. Amer. Meteor. Soc.* **77**, 869882.

Behrenfeld, M. (2010), 'Abandoning Sverdrup's Critical Depth Hypothesis on phytoplankton blooms', *Ecology* **91**, 977–989.

Behrenfeld, M. J. and Boss, E. S. (2014), 'Resurrecting the ecological underpinnings of ocean plankton blooms', *Annual Review of Marine Science* **6**(1), 167–194.

Bishop, J. K. B., Wood, T. J., Davis, R. E. and Sherman, J. T. (2004), 'Robotic observations of enhanced carbon biomass and export at 55 degrees S during SOFeX', *Science* **304**(5669), 417–420.

Bonjean, F. and Lagerloef, G. S. E. (2002), 'Diagnostic model and analysis of the surface currents in the tropical Pacific Ocean', *Journal of Physical Oceanography* **32**, 2938–2954.

Boss, E. and Pegau, W. S. (2001), 'Relationship of light scattering at an angle in the backward direction to the backscattering coefficient', *Appl. Opt.* **40**(30), 5503–5507.

Boyd, P. W., Watson, A. J., Law, C. S., Abraham, E. R., Trull, T., Murdoch, R., Bakker, D. C. E., Bowie, A. R., Buesseler, K. O., Chang, H., Charette, M., Croot, P., Downing, K., Frew, R., Gall1, M., Hadfield, M., Hall, J., Harvey, M., Jameson, G., LaRoche, J., Liddicoat, M., Ling, R., Maldonado, M. T., McKay, R. M., Nodder, S., Pickmere, S., Pridmore, R., Rintoul, S., Safi, K., Sutton, P., Strzepek, R., Tanneberger, K., Turner, S., Waite, A. and Zeldis, J. (2000), 'A mesoscale phytoplankton bloom in the polar Southern Ocean stimulated by iron fertilization', *Nature* **407**, 695–702.

Briggs, N., Perry, M. J., CetiniC, I., Lee, C., D'Asaro, E., Gray, A. M. and Rehm, E. (2011), 'High-resolution observations of aggregate flux during a sub-polar North Atlantic spring bloom', *Deep Sea Research Part I: Oceanographic Research Papers* **58**(10), 1031 – 1039.

Ciais, P., Sabine, C., Bala, G., Bopp, L., Brovkin, V., Canadell, J., Chhabra, A., DeFries, R., Galloway, J., Heimann, M., Jones, C., Qur, C. L., Myneni, R., Piao, S. and Thornton, P. (2013), Carbon and other biogeochemical cycles, *in* T. F. Stocker, Q. D, G. K. Plantter, M. Tignor, S. K. Allen, J. Boschung, A. Nauels, Y. Xia, V. Bex and P. M. Midgley, eds, 'Climate Change 2013: The Physical Science Basis. Contribution of Working Group I to the Fifth Assessment Report of the Intergovernmental Panel on Climate Change', Columbia Univ. Press, United Kingdom and New York, NY, USA.

Coale, K. H., Johnson, K. S., Chavez, F. P., Buesseler, K. O., Barber, R. T., Brzezinski, M. A., Cochlan, W. P., Millero, F. J., Falkowski, P. G., Bauer, J. E., Wanninkhof, R. H., Kudela, R. M., Altabet, M. A., Hales, B. E., Takahashi, T., Landry, M. R., Bidigare, R. R., Wang, X., Chase, Z., Strutton, P. G., Friederich, G. E., Gorbunov, M. Y., Lance, V. P., Hilting, A. K., Hiscock, M. R., Demarest, M., Hiscock, W. T., Sullivan, K. F., Tanner, S. J., Gordon, R. M., Hunter, C. N., Elrod, V. A., Fitzwater, S. E., Jones, J. L., Tozzi, S., Koblizek, M., Roberts, A. E., Herndon, J., Brewster, J., Ladizinsky, N., Smith, G., Cooper, D., Timothy, D., Brown, S. L., Selph, K. E., Sheridan, C. C., Twining, B. S. and Johnson, Z. I. (2004), 'Southern Ocean Iron Enrichment Experiment: Carbon cycling in high- and low-Si waters', *Science* **304**(5669), 408–414.

Comiso, J. C., McClain, C. R., Sullivan, C. W., Ryan, J. P. and Leonard, C. L. (1993), 'Coastal zone color scanner pigment concentrations in the Southern Ocean and relationships to geophysical surface features', *Journal of Geophysical Research: Oceans* **98**(C2), 2419–2451.

Daniault, N. and Menard, Y. (1985), 'Eddy kinetic energy distribution in the Southern Ocean from altimetry and fgge drifting buoys', *Journal of Geophysical Research: Oceans* **90**(C6), 11877–11889.

Dong, S., Sprintall, J., Gille, S. T. and Talley, L. (2008), 'Southern Ocean mixed-layer depth from Argo float profiles', *Journal of Geophysical Research: Oceans* **113**(C6).

Einstein, A. (1910), 'Theorie der Opaleszenz von homogenen Flssigkeiten und Flssigkeitsgemischen in der Nhe des kritischen Zustandes', *Annalen der Physik* **338**(16), 1275–1298.

El-Sayed, S. (1987), Productivity of the Antarctic Waters–a reappraisal, *in* O. Holm-Hansen, L. Bolis and R. Gilles, eds, 'Marine Phytoplankton and Productivity', Springer-Verlag, Berlin, Germany, pp. 19–34.

Eppley, R. W. (1972), 'Temperature and phytoplankton growth in the sea', *Fishery Bulletin* **70**(4), 1068–1085.

Falkowski, P. G. (1983), 'Light-shade adaptation and vertical mixing of marine phytoplankton: A comparative field study', *Journal of Marine Research* **41**(2), 215–237.

Falkowski, P. and Raven, J., eds (2007), *Aquatic Photosynthesis*, Princeton University Press.

Farmer, D. M., McNeil, C. L. and Johnson, B. D. (1993), 'Evidence for the importance of bubbles in increasing airsea gas flux', *Nature* **361**, 620 – 623.

Fischer, G. and Karakas, G. (2009), 'Sinking rates and ballast composition of particles in the atlantic ocean: implications for the organic carbon fluxes to the deep ocean', *Biogeosciences* **6**(1), 85–102.

Garcia, H. E., Locarnini, R. A., Boyer, T. P., Antonov, J. I., Zweng, M. M., Baranova, O. K. and Johnson, D. R. (2009), Nutrients (phosphate, nitrate, silicate), *in* S. Levitus, ed., 'World Ocean Atlas 2009', Vol. 4, NOAA Atlas NESDIS 71, U.S. Government Printing Office, Washington, D.C., p. 398.

Gervais, F., Riebesell, U. and Gorbunov, M. Y. (2002), 'Changes in primary productivity and chlorophyll-a in response to iron fertilization in the Southern Polar Frontal Zone', *Limnology and Oceanography* **47**(5), 1324–1335.

Gill, A. E. (1982), Appendix Three - Properties of Seawater, *in* 'AtmosphereOcean Dynamics', Vol. 30 of *International Geophysics*, Academic Press, pp. 599 – 603.

Gordon, A. L., Georgi, D. T. and Taylor, H. W. (1977), 'Antarctic Polar Frontal Zone in the Western Scotia Sea – Summer 1975', *Journal of Physical Oceanography* **7**, 309328.

Gruber, N., Gloor, M., Fletcher, S. M., Doney, S., Dutkiewicz, S., Follows, M., Gerber, M., Jacobson, A., Joos, F., Lindsay, K., Menemenlis, D., Mouchet, A., Muller, S., Sarmiento, J. and Takahashi, T. (2009), 'Oceanic sources, sinks and transport of atmospheric CO_2', *Global Biochemical Cycles* **23**.

Ho, D. T., Wanninkhof, R., Schlosser, P., Ullman, D. S., Hebert, D. and Sullivan, K. F. (2011), 'Toward a universal relationship between wind speed and gas exchange: Gas transfer velocities measured with 3He/SF6 during the Southern Ocean Gas Exchange Experiment', *Journal of Geophysical Research: Oceans* **116**(C4).

Hoffmann, L. J., Peeken, I., Lochte, K., Assmy, P. and Veldhuis, M. (2006), 'Different reactions to Southern Ocean phytoplankton size classes to iron fertilization', *Science* **51**(3), 1217–1229.

Holm-Hansen, O., Kahru, M. and Hewes, C. D. (2005), 'Deep chlorophyll a maxima (DCMs) in pelagic Antarctic waters. ii. relation to bathymetric features and dissolved iron concentrations', *Marine Ecology-Progress Series* **297**, 71–81.

Huisman, J., van Oostveen, P. and Weissing, F. (1999), 'Critical depth and critical turbulence: Two different mechanisms for the development of phytoplankton blooms', *Limnology and Oceanography* **44**(7), 1781–1787.

IPCC (2013), Summary for policymakers, *in* T. F. Stocker, Q. D, G. K. Plantter, M. Tignor, S. K. Allen, J. Boschung, A. Nauels, Y. Xia, V. Bex and P. M. Midgley, eds, 'Climate Change 2013: The Physical Science Basis. Contribution of Working Group I to the Fifth Assessment Report of the Intergovernmental Panel on Climate Change', Columbia Univ. Press, United Kingdom and New York, NY, USA.

Johnson, G. C. (2001), 'The Pacific Ocean subtropical cell surface limb', *Geophysical Research Letters* **28**(9), 1771–1774.

Kalnay, E., Kanamitsu, M., Kistler, R., Collins, W., Deaven, D., Gandin, L., Iredell, M., Saha, S., White, G., Woollen, J., Zhu, Y., Leetmaa, A., Reynolds, R., Chelliah, M., Ebisuzaki, W., Higgins, W., Janowiak, J., Mo, K. C., Ropelewski, C., Wang, J., Jenne, R., and Joseph, D. (1996), 'The NCEP/NCAR 40-year reanalysis project', *Bull. Amer. Meteor. Soc.* **77**, 437–471.

Klunder, M. B., Laan, P., Baar, H. J. W. D., Middag, R., Neven, I. and Ooijen, J. V. (2014), 'Dissolved Fe across the Weddell Sea and Drake Passage: impact of DFe on nutrient uptake', *Biogeosciences* **11**(3), 651–669.

Lagerloef, G. S. E., Mitchum, G. T., Lukas, R. B. and Niiler, P. P. (1999), 'Tropical Pacific near-surface currents estimated from altimeter, wind, and drifter data', *Journal of Geophysical Research: Oceans* **104**(C10), 23313–23326.

Large, W. G. and Pond, S. (1981), 'Open ocean momentum flux measurements in moderate to strong winds', *J. Phys. Oceanogr.* **11**, 324–336.

Maffione, R. A. and Dana, D. R. (1997), 'Instruments and methods for measuring the backward-scattering coefficient of ocean waters', *Appl. Opt.* **36**(24), 6057–6067.

Martin, J. H. (1990), 'Glacial-interglacial CO_2 change: The Iron Hypothesis', *Paleoceanography* **5**(1), 1–13.

Martin, J. H., Gordon, R. M. and Fitzwater, S. E. (1990), 'Iron in Antarctic waters.', *Nature* **345**, 156–159.

McNeil, B. I., Metzl, N., Key, R. M., Matear, R. J. and Corbiere, A. (2007), 'An empirical estimate of the Southern Ocean air-sea CO_2 flux', *Global Biogeochemical Cycles* **21**(3).

Moore, J. K. and Abbott, M. R. (2000), 'Phytoplankton chlorophyll distributions and primary production in the Southern Ocean', *Journal of Geophysical Research* **105**(C12), 28709–28722.

Moore, J. K. and Abbott, M. R. (2002), 'Surface chlorophyll concentrations in relation to the Antarctic Polar Front: seasonal and spatial patterns from satellite observations', *Journal of Marine Systems* **37**(13), 69 – 86.

Moore, J. K., Abbott, M. R., Richman, J. G., Smith, W. O., Cowles, T. J., Coale, K. H., Gardner, W. D. and Barber, R. T. (1999), 'SeaWiFS satellite ocean color data from the Southern Ocean', *Geophysical Research Letters* **26**(10), 1465–1468.

Nolting, R. F., Baar, H. J. W. D., Bennekom, A. J. V. and Masson, A. (1991), 'Cadmium, copper and iron in the Scotia Sea, Weddell Sea and Weddell/Scotia Confluence (Antarctica)', *Marine Chemistry* **35**(14), 219 – 243.

Nowlin, W., Pillsbury, R. D. and Bottero, J. (1981), 'Observations of kinetic energy levels in the antarctic circumpolar current at Drake Passage', *Deep Sea Research Part A. Oceanographic Research Papers* **28**(1), 1 – 17.

Orr, J. C., Maier-Reimer, E., Mikolajewicz, U., Monfray, P., Sarmiento, J. L., Toggweiler, J. R., Taylor, N. K., Palmer, J., Gruber, N., Sabine, C. L., Quere, C. L., Key, R. M. and Boutin, J. (2001), 'Estimates of anthropogenic carbon uptake from four three-dimensional global ocean models', *Global Biogeochemical Cycles* **15**(1), 43–60.

Orsi, A. H., Whitworth, T. and Nowlin, W. D. (1995), 'On the meridional extent and fronts of the Antarctic Circumpolar Current', *Deep Sea Research Part I: Oceanographic Research Papers* **42**(5), 641 – 673.

Raven, J. and Falkowski, P. (1999), 'Oceanic sinks for atmospheric CO_2', *Plant, Cell, and Enviroment* **22**, 741–755.

Reynolds, R. W. and Smith, T. M. (1994), 'Improved global sea surface temperature analyses using optimum interpolation', *J. Climate* **7**, 929948.

Roy, T., Rayner, P., Matear, R. and Francey, R. (2003), 'Southern hemisphere ocean CO_2 uptake: reconciling atmospheric and oceanic estimates', *Tellus B* **55**(2), 701–710.

Sabine, C. L., Feely, R., Gruber, N., Key, R. M., Lee, K., Bullister, J. L., Wanninkhof, R., Wong, C. S., Wallace, D. W. R., Tilbrook, B., Millero, F. J., Peng, T., Kozyr, A., Ono, T. and Rios, A. F. (2004), 'The oceanic sink for anthropogenic CO_2', *Science* **305**(5682), 367–371.

Sarmiento, J. L., Hughes, T. M. C., Stouffer, R. J. and Manade, S. (1998), 'Simulated response of the ocean carbon cycle to anthropogenic climate warming', *Nature* **393**, 245–249.

Smetacek, V., Klaas, C., Strass, V. H., Assmy, P., Montresor, M., Cisewski, B., Savoye, N., Webb, A., dOvidio, F., Arrieta, J. M., Bathmann, U., Bellerby, R., Berg, G. M., Croot, P., Gonzalez, S., Henjes, J., Herndl, G. J., Hoffmann, L. J., Leach, H., Losch, M., Mills, M. M., Neill, C., Peeken, I., Rottgers, R., Sachs, O., Sauter, E., Schmidt, M. M., Schwarz, J., Terbruggen, A. and Wolf-Gladrow, D. (2012), 'Deep carbon export from a Southern Ocean iron-fertilized diatom bloom', *Nature* **487**, 313–319.

Sokolov, S. and Rintoul, S. R. (2007), 'On the relationship between fronts of the Antarctic Circumpolar Current and surface chlorophyll concentrations in the Southern Ocean', *Journal of Geophysical Research: Oceans* **112**(C7).

Stahlke, D. (2014), Personal Communication–Email Correspondence.

Sullivan, J. M., Twardowski, M., Ronald, J., Zaneveld, V. and Moore, C. C. (2013), Measuring optical backscattering in water, *in* 'Light Scattering Reviews 7', Springer Praxis Books, Springer Berlin Heidelberg, pp. 189–224.

Sullivan, J. M. and Twardowski, M. S. (2009), 'Angular shape of the oceanic particulate volume scattering function in the backward direction', *Appl. Opt.* **48**(35), 6811–6819.

Sverdrup, H. U. (1953), 'On conditions for the vernal blooming of phytoplankton', *Journal du Conseli International pour l'Exploration de la Mer* **18**(3), 287–295.

Takahashi, T., Feely, R., Weiss, R., Wanninkhof, R., Chimpan, D., Sutherland, S. and Takashashi, T. (1997), 'Global sea-air flux of CO_2: An estimate based on measurements of air-sea pCO_2 difference', *Procedings of the National Academy of Science* **94**, 8292–8299.

Takahashi, T., Sutherland, S. C., Sweeney, C., Poisson, A., Metzl, N., Tilbrook, B., Bates, N., Wanninkhof, R., Feely, R. A., Sabine, C., Olafsson, J. and Nojiri, Y. (2002), 'Global sea–air CO_2 flux based on climatological surface ocean pCO_2, and seasonal biological and temperature effects', *Deep Sea Research Part II: Topical Studies in Oceanography* **49**(910), 1601 – 1622.

Taylor, J. R. and Ferrari, R. (2011), 'Shutdown of turbulent convection as a new criterion for the onset of spring phytoplankton blooms', *Limnology and Oceanography* **56**(6), 2293–2307.

Thompson, A. F. and Gille, S. T. (2007), 'Spatial and temporal patterns of small-scale mixing in Drake Passage', *Journal of Physical Oceanography* **37**, 572592.

Turner, J. T. (2002), 'Zooplankton fecal pellets, marine snow and sinking phytoplankton blooms', *Aquatic Microbial Ecology* **27**, 57–102.

Twardowski, M. S. (2014), Personal Communication–Email Correspondence.

Twining, B. S., Baines, S. B. and Fisher, N. S. (2004), 'Element stoichiometries of individual plankton cells collected during the Southern Ocean Iron Experiment (SOFeX)', *Limnol. Oceanogr.* **46**(6), 2115–2128.

Venables, H. and Moore, C. M. (2010), 'Phytoplankton and light limitation in the Southern Ocean: Learning from high-nutrient, high-chlorophyll areas', *Journal of Geophysical Research: Oceans* **115**(C2).

Webb Research, T. (2012), *APEX Profiler User Manual*, Teledyne Webb Research, A Teledyne Instruments, Inc. Company, 82 Technology Park Drive, E. Falmouth Massachusetts 02536.

Zhang, X., Hu, L. and He, M. (2009), 'Scattering by pure seawater: Effect of salinity', *Opt. Express* **17**(7), 5698–5710.